

PAIR PRODUCTION AND COMPTON SCATTERING IN COMPACT SOURCES AND
COMPARISON TO OBSERVATIONS OF ACTIVE GALACTIC NUCLEI

ALAN P. LIGHTMAN

Harvard-Smithsonian Center for Astrophysics

AND

ANDRZEJ A. ZDZIARSKI

California Institute of Technology, and Harvard-Smithsonian Center for Astrophysics

Received 1986 November 14; accepted 1987 February 3

ABSTRACT

We determine the steady state particle and photon distributions under the assumption of continuous injection of relativistic electrons and low-energy photons throughout a spherical volume. Through inverse Compton scattering, the primary electrons produce γ -rays, which then produce electron-positron pairs. The pairs constitute a secondary electron injection, and the process continues, with each generation of pairs cooling down to subrelativistic energies before thermalizing and annihilating. We improve on earlier investigations of this problem, compute detailed emergent spectra for a wide range of parameters, and compare our results to the data from active galactic nuclei (AGNs). The range of observed spectra and inferred high-energy cutoffs can be fitted by varying the input parameters of the injected particles and photons, subject to certain constraints. In general, pairs are less important in these models than previously thought. For the sizes of AGNs inferred from time variability, pair production cannot provide a break in the γ -ray spectra at energies below ~ 1 – 5 MeV, as required by the limits of the γ -ray background; the break must be achieved instead by suitable constraints on the primary injections of electrons and photons. Furthermore, pairs may provide only a minor contribution to the X-ray and γ -ray spectra. However, pairs can still greatly outnumber ionization electrons, even at modest luminosities, and pairs may limit the maximum luminosities of AGNs by reducing the effective Eddington limit.

Subject headings: gamma rays: general — particle acceleration — radiation mechanisms

I. INTRODUCTION AND SUMMARY

Two decades ago, it was pointed out that γ -rays produced in sufficiently luminous and compact astrophysical objects would create electron-positron pairs by collisions with lower energy photons (Jelley 1966; Herterich 1974), $\gamma + \gamma \rightarrow e^+ + e^-$. This process both depletes the escaping radiation at high energies and also changes the composition and properties of the radiating gas through the injection of new particles. An approximate condition for such pair creation to become significant is that a sizable fraction of the radiation from the object be emitted above the electron rest mass energy, $m_e c^2 = 511$ keV, and that the “compactness parameter” of the object, $l \equiv L\sigma_T/(Rm_e c^3)$, exceed 10, where L is the total luminosity, R is a characteristic source dimension, and σ_T is the Thomson cross section. When $l \gg 10$, a photon of energy $m_e c^2$ has an optical depth of unity for creating pairs.

Both theoretical arguments and observational evidence suggest that pair production may be important in active galactic nuclei (AGNs) and quasars (QSOs), especially in the vicinity of a central black hole. On the theoretical side, we note that the compactness parameter may be rewritten as

$$l = \frac{L\sigma_T}{Rm_e c^3} \quad (1a)$$

$$= 2\pi \left(\frac{m_p}{m_e}\right) \left(\frac{L}{L_E}\right) \left(\frac{R_S}{R}\right), \quad (1b)$$

where m_p/m_e is the ratio of proton to electron mass, $L_E \equiv 4\pi GMcm_p/\sigma_T$ is the Eddington limit, and $R_S \equiv 2GM/c^2$ is the

Schwarzschild radius of a black hole of mass M . Thus, for $R \sim 10R_S$, typical of many accretion models, l will reach 10 for a modest value of L/L_E . Furthermore, in accreting onto a black hole, each proton can convert of order 10% of its rest mass into energy, making available $\sim 0.1m_p c^2 \sim 100m_e c^2$ of energy per ionization electron in the gas. Shock waves, magnetic reconnection, and strong electric fields may continuously accelerate a small fraction of electrons up to much higher energies. If such electrons can produce photons of similar energies, e.g., through synchrotron emission or Compton scattering, then the conditions for copious pair production are satisfied.

On the observational side, the compactness parameters and pair-production optical depths of AGNs and QSOs may be estimated by assuming that time variabilities give characteristic sizes, $R \lesssim c\Delta t$, where Δt is the observed time scale of variability. Recent data from AGNs and QSOs (see Wandel and Mushotzky 1986, and references therein, and Table 3 below) indicate that a large fraction of these objects have $l \approx 10$. The spectra from AGNs and QSOs extend up to 0.1–5 MeV (e.g., Mushotzky 1982; Schönfelder 1983; Rothschild *et al.* 1983; Petre *et al.* 1984; Graml, Penningsfeld, and Schönfelder 1978; Hall *et al.* 1976; Perotti *et al.* 1981a, b; von Ballmoos, Diehl, and Schönfelder 1987; Bignami *et al.* 1979; Damle *et al.* 1986) and possibly higher, although only a few objects are bright enough to have been seen at energies above a few hundred keV with current detector sensitivities. Among those objects detected are Cen A, NGC 4151, MCG 8–11–11, and 3C 120, which have high-energy breaks at 3–10 MeV (Graml, Penningsfeld, and Schönfelder 1978; Perotti *et al.* 1981a, b; Bignami *et al.* 1979; von Ballmoos, Diehl, and

Schönfelder 1987; Damle *et al.* 1986). Pair annihilation features have not yet been observed. In summary, the current observational evidence for pair processes in AGNs is suggestive but not conclusive, and a closer comparison between data and theory is needed, which we attempt below.

Most theoretical investigations of pair processes in recent years have followed the fruitful suggestion of Guilbert, Fabian, and Rees (1983) that electrons are continuously injected into the emitting region with a high-energy, nonthermal distribution and then produce γ -ray photons, either through synchrotron emission or Compton scattering. The γ -rays produce pairs, which constitute a secondary electron injection and produce additional high-energy photons. Depending on parameters, further generations of particles and photons may be produced. As a result of rapid cooling (the cooling time of an electron of Lorentz factor γ is $\sim [R/c]/[\gamma l] \ll R/c$), the electrons and positrons cool down to subrelativistic energies before thermalizing and annihilating. Thus, except for the scattering effects of the population of low-energy thermal pairs about to annihilate, the process is essentially nonthermal. This contrasts to previous calculations, which assumed all the particles to have a Maxwellian steady state distribution (see, e.g., Svensson 1986 for a review).

Following the above physical picture, we first studied the self-consistent distribution of particles and photons under the assumptions that higher order Compton scatterings and the scattering effects of the low-energy thermal pairs could be neglected (Zdziarski and Lightman 1985, hereafter ZL85). For a monoenergetic injection of primary electrons, the photon energy spectral index α in the X-ray region of the spectrum increases from $\alpha \approx 0.5$ (when pairs are unimportant) to $\alpha \approx 0.9$ (when pairs are very important) as the compactness parameter l increases from 0.1 to 100. When the number of pair generations is large and the medium is thick to pair production at all relevant energies and the effects of thermal scattering can be neglected, the pairs are produced with a rate $\propto \gamma^{-2}$, and the index α approaches unity, as first discussed by Kazanas (1984). For a power-law injection of primary electrons, $Q(\gamma) \propto \gamma^{-\Gamma}$, where Q is the rate of production of electrons per unit energy per unit volume, the first-order scattering by pairs steepen the X-ray spectrum from $\alpha = \Gamma/2$ toward unity, as long as $\Gamma < 2$ (when the primary electron injection is flatter than the pair injection). The case of monoenergetic electron injection was further studied by Fabian *et al.* (1986, hereafter FBGPC86) and by Svensson (1987, hereafter S87), who significantly extended the treatment of ZL85 by including the scattering effects of the thermal pairs, which become important at compactness parameters $l \gtrsim 30$. Furthermore, S87 has derived a number of new analytical results regarding the pair generations and production rates.

In the present investigation, we further improve on the theory, calculate many models with monoenergetic and power-law electron injections spanning a large range of input parameters, and make detailed comparisons of our results to the observed data of AGNs and QSOs. We extend the theory by using the full Kompaneets equation to treat thermal Comptonization up to mildly relativistic energies and by adding relativistic corrections to photon scattering and escape probabilities. We also calculate the ratio of pairs to ionization electrons in accretion models and propose that a coupling between pairs and protons can reduce the Eddington limit.

Our main results and conclusions are the following:

1. Relativistic corrections to the scattering and escape prob-

abilities are very important when the Thomson depth τ_T is large. For $\tau_T \approx 10$, for example, these corrections reduce the *effective* value of the scattering depth to ~ 1 at energies just below $m_e c^2$, with a corresponding large effect on the spectrum.

2. In accretion models, the ratio of pairs to ionization electrons can be large, in contrast to previous results for thermal production of pairs.

3. Both the observations of AGNs and the theory indicate a large range of parameters from one object to the next, with no "universal" AGN. AGNs and QSOs have X-ray (2–10 keV) spectral indices α in the range of ~ 0.4 –1.0 and "observed X-ray compactness parameters" $l_{\text{ob}} \equiv L_x \sigma_T / \Delta t m_e c^4$ in the range $\sim 3 \times 10^{-2}$ –10 (see Figs. 11 and 12).

4. The required high-energy break in the spectrum of a typical AGN, with $l_{\text{ob}} \approx 0.5$, is probably not caused by pair production, but rather by a small value of the maximum energy of the scattered photons or by a low ratio of input photon power to input primary electron power. In the first class of models, the range of observed spectral indices corresponds to a range in the power-law indices of the primary injected electrons; in the second class, it corresponds to a range in the ratio of injected soft photon power to injected primary electron power. Each of these classes of models can fit most of the observed data. Pairs do not play an important role in models for the typical AGN.

5. Electron-positron pairs increase the Thomson opacity of a black hole photosphere and can reduce the effective Eddington luminosity if they are coupled to the protons. The observed upper limit $l_{\text{ob}} \lesssim 10$ for AGNs might be explained by this "pair-reduced Eddington limit," which, depending on conditions, is ~ 10 times lower than the classical Eddington limit.

II. PHYSICAL PROCESSES IN PAIR PLASMAS

a) Fundamental Assumptions and Parameters

We assume that electrons are continuously injected at a rate $Q(\gamma)$ particles per unit time per unit volume per unit energy, with $\gamma_{\text{min}} \leq \gamma \leq \gamma_{\text{max}}$. When $Q(\gamma)$ is a power law, we take $Q = Q_0 \gamma^{-\Gamma}$. This injection occurs uniformly throughout a spherical volume of radius R and is measured by the dimensionless "electron compactness parameter" (see eq. [1a]),

$$l_e = \frac{L_e \sigma_T}{R m_e c^3} = \frac{4\pi R^2 \sigma_T}{3c} \int Q(\gamma)(\gamma - 1) d\gamma, \quad (2a)$$

where

$$L_e = (4\pi R^3/3) m_e c^2 \int Q(\gamma)(\gamma - 1) d\gamma$$

is the total power put into the electrons. We assume also that soft photons are injected at the rate $\dot{n}_0(x)$ photons per unit time per unit volume per unit energy x , where $x \equiv h\nu/m_e c^2$ is the dimensionless photon energy. We will take $\dot{n}_0(x)$ to be a blackbody, peaked at energy $x = x_s$ (where x_s is related to the blackbody temperature T_{bb} by $x_s = 2.8kT_{\text{bb}}/m_e c^2$), which may be identified with the "UV bump" observed in some AGNs (Malkan and Sargent 1982; Elvis *et al.* 1986; Bechtold *et al.* 1987). Accordingly, we take x_s in the range 10^{-5} – 10^{-4} . We will assume $x_s \gamma_{\text{max}} < \frac{3}{4}$, so that for any electron a nonzero part of the photon spectrum is in the Thomson limit (see eq. [8]). Allowing $\dot{n}_0(x)$ to be a smooth distribution peaked at x_s , rather than a δ -function, as was assumed by ZL85, S87, and FBGPC86, smoothes out some of the artificially sharp spectral features found in the latter calculations. The "soft photon

compactness parameter" is

$$l_s = \frac{4\pi R^2 \sigma_T}{3c} \int \dot{n}_0(x) x dx. \quad (2b)$$

If $\dot{n}_0(x)$ is identified with the "UV bump" and this emission comes from within the same region as the X-ray and γ -ray emission, then the observations indicate $0.05 \lesssim l_s/l_e \lesssim 0.5$ ($1 \lesssim l_s/l_x \lesssim 10$ and $l_x/l_e \sim 0.05$).

For a monoenergetic injection, $Q(\gamma) = Q_0 \delta(\gamma - \gamma_{\max})$, the four dimensionless parameters that specify a model are x_s , γ_{\max} , l_e , and l_s/l_e . For a power-law electron injection, γ_{\min} and Γ must also be specified. We will take $\gamma_{\min} = 1$ in all of our detailed calculations.

We note here that our compactness parameter, as defined by equation (1a), is the same as in ZL85 and in S87, but is $4\pi/3$ times that in FBGPC86. Our l_e is denoted by l_i in S87 and our l_s/l_e is denoted by $\dot{U}^{\text{rad}}/\dot{U}^{\text{el}}$ in FBGPC86.

Electrons are assumed to cool by scattering lower energy photons, which may either come from the injected distribution $\dot{n}_0(x)$ (first-order scattering) or from previously scattered photons (higher order scatterings). Once x_s , γ_{\max} , l_e , and l_s/l_e (and γ_{\min} and Γ if the electron injection is a power law) have been specified, the particle and photon distributions may be self-consistently determined under the combined processes of pair production and annihilation, inverse Compton scattering off electrons and positrons (which exist in both nonthermal and thermal populations), and photon escape. We assume that particles do not escape.

For purposes of comparison to observations, two other compactness parameters must be defined: the "X-ray compactness parameter,"

$$l_x \equiv \frac{L_x \sigma_T}{R m_e c^3}, \quad (2c)$$

and the "observed compactness parameter,"

$$l_{\text{ob}} \equiv \frac{L_x \sigma_T}{\Delta t m_e c^4}. \quad (2d)$$

Here L_x is the luminosity in the 2–10 keV energy range and Δt is the shortest observed time scale of variability. If τ_T is the Thomson scattering depth, then we may take $\Delta t \gtrsim (R/c)(1 + \tau_T/3)$ (see eqs. [18a], [18b]). Taking this relation as an equality, we have

$$l_{\text{ob}} = l_x / (1 + \tau_T/3). \quad (2e)$$

The right-hand side of equation (2e) will be calculated in our models, while the left-hand side can be measured.

b) Steady State Kinetic Equations

The electron distribution will be divided into a thermal and a nonthermal population. Let $n(x)$ and $N(\gamma)$ be the number densities per unit energy of photons and nonthermal particles, respectively, at a representative interior point of the emission region. Then the steady state equations are

$$0 = \dot{n}_0 + \dot{n}_A + \dot{n}_C^{\text{NT}} + \dot{n}_C^T - \frac{c}{R} n(\tau_C^{\text{NT}} + \tau_{\gamma\gamma}) - \dot{n}_{\text{esc}}, \quad (3)$$

$$0 = \dot{N}_C(\gamma) + P(\gamma) + Q(\gamma). \quad (4)$$

Here \dot{n}_0 , \dot{n}_A , \dot{n}_C^{NT} , and \dot{n}_C^T are the rate of production of photons

at energy x by soft photon injection, pair annihilation, Compton scattering off nonthermal electrons, and Compton scattering off thermal electrons, respectively. (The scattering by thermal and nonthermal electrons will be treated separately.) Photons are removed by Compton scattering with nonthermal electrons, having optical depth τ_C^{NT} , by pair creation, having optical depth $\tau_{\gamma\gamma}$, and by escape from the region, at a rate of \dot{n}_{esc} . The removal of photons at energy x by scattering with thermal electrons is included in \dot{n}_C^T . In the electron equation, $\dot{N}_C(\gamma)$ is the rate of change of the particle distribution at energy γ via nonthermal Compton scattering, $P(\gamma)$ is the rate of pair creation per unit volume per unit energy, and $Q(\gamma)$ is the rate of injection of primary electrons per unit volume per unit energy. At low energies, $\gamma \sim 1$, the electrons and positrons are assumed to thermalize and form a Maxwell-Boltzmann distribution at temperature $\Theta \equiv kT/m_e c^2 \ll 1$ before annihilating. The density and temperature of this thermal population of electrons will be determined below and will then be used in calculating \dot{n}_C^T in equation (3).

In the rest of this section, we evaluate the processes in equations (3) and (4). In Appendix A, we demonstrate that our equations conserve energy; in Appendix B, we discuss the numerical method used in their solution.

c) The Steady State Nonthermal Electron Distribution

Using the continuity equation for the nonthermal electron distribution,

$$\dot{N}_C(\gamma) = -\frac{\partial}{\partial \gamma} [\dot{\gamma} N(\gamma)], \quad (5)$$

equation (4) may be formally integrated to yield

$$N(\gamma) = -\dot{\gamma}^{-1} \int_{\gamma}^{\gamma_{\max}} [Q(\gamma') + P(\gamma')] d\gamma'. \quad (6)$$

Here $\dot{\gamma}$, the rate of cooling of an electron of Lorentz factor γ via Compton scattering, is

$$\dot{\gamma} = -\sigma_T c \left(\frac{4}{3} \gamma^2 - 1 \right) \int_0^{3/4\gamma} n(x') x' dx'. \quad (7)$$

In deriving equation (7), we have assumed that a photon of energy x' scattering off an electron of energy γ emerges with energy

$$x = \frac{4}{3} \gamma^2 x', \quad (8)$$

and that this process occurs with the Thomson cross section at all photon energies satisfying $x'\gamma \leq \frac{3}{4}$. For larger photon energies, we assume the cross section is zero. Equations (6) and (7) are the same as equation (9) in FBGPC86, except that the latter replace $4/3$ by 1 . By including the full $n(x)$ in equation (7), and not just the contribution from soft photons at energy $\sim x_s$, second- and higher order Compton scatterings are allowed in a self-consistent manner, in contrast to the treatments in ZL85, considering the first-order scattering only, and in S87, treating the second-order scattering as a perturbation not affecting the electron distribution $N(\gamma)$.

d) Photon Production and Absorption by Nonthermal Compton Scattering

Using the approximation in equation (8) and the discussion below it, the photon production by nonthermal Compton scat-

tering may be written as

$$\begin{aligned} \dot{n}_c^{\text{NT}}(x) &= c\sigma_T \int n(x') dx' \delta\left(x - \frac{4}{3}\gamma^2 x'\right) N(\gamma) H\left(\frac{3}{4} - x'y\right) dy \\ &= \frac{3^{1/2}}{4} c\sigma_T x^{-1/2} \int_{\sqrt{3x/4\gamma^2_{\text{max}}}}^{\min(3/4x, 3x/4)} n(x') x'^{-1/2} N\left(\sqrt{\frac{3x}{4x'}}\right) dx', \end{aligned} \quad (9)$$

where $H(y) = 1$ for $y > 0$ and 0 for $y < 0$.

Equation (9) is analogous to equation (6) in FBGPC86, and, again, it differs from the corresponding equation in ZL85 by its inclusion of higher order scatterings. S87 includes the second-order scattering as a perturbation (see § IIc).

The absorption depth corresponding to this process, under our assumptions, may be simply written as

$$\tau_c^{\text{NT}}(x) = \sigma_T R \int_1^{3/4x} N(\gamma) d\gamma. \quad (10)$$

e) Pair Production and Annihilation

i) Absorption Depth to Pair Production

In pair production, photons of energy x interact primarily with photons of energy $\sim 1/x$. Using the calculations of Gould and Schröder (1967) for a power-law radiation field $n(x) \propto x^{-(\alpha+1)}$, the pair-production absorption depth may be written as

$$\tau_{\gamma\gamma}(x) = \eta(\alpha) R \sigma_T \frac{1}{x} n\left(\frac{1}{x}\right), \quad (11)$$

where $\eta(\alpha) = 0.24$ and 0.12 for $\alpha = 0.5$ and 1 , respectively. Following S87, we take $\eta = 0.2$ for our calculations. This approximation differs slightly from that of FBGPC86, where the cross section is approximated as a rectangular function and then integrated over the photon distribution.

ii) Rate of Pair Production

In pair production we assume that the incoming energy is shared equally between the electron and positron, each of Lorentz factor γ . Thus energy conservation requires

$$x + \frac{1}{x} = 2\gamma. \quad (12)$$

For every photon that disappears at an energy $x \geq 1$, two particles are produced. Thus we may write

$$\int_{\gamma}^{\gamma_{\text{max}}/2} P(\gamma) d\gamma = \frac{2c}{R} \int_{\gamma}^{\gamma_{\text{max}}} n(x) \tau_{\gamma\gamma}(x) dx, \quad (13)$$

where the lower limit on the right-hand side of equation (13) is obtained by taking the $x > 1$ root of equation (12). Equation (13) differs from the corresponding equations in ZL85 and in S87, where the energy input of the $x \leq 1$ photon is ignored in equation (12), and radiative transfer is treated differently (e.g., compare eq. [13] with eq. [2.18] in S87).

iii) Pair Yield

To measure the efficiency of putting energy into the rest mass of pairs we will define the "pair yield" (see Guilbert, Fabian, and Rees 1983; S87; FBGPC86)

$$\text{PY} \equiv \frac{\int_1^{\gamma_{\text{max}}/2} P(\gamma) d\gamma}{\int_1^{\gamma_{\text{max}}} Q(\gamma)(\gamma - 1) d\gamma}. \quad (14)$$

As first found by S87, and confirmed by our calculations, for $\Gamma \ll 2$, PY increases rapidly in the range $2 \lesssim l_e \lesssim 7$ and approaches a maximum of ~ 0.1 for $l_e \gg 10$, independent of other parameters (see Fig. 8). In the three references above, the pair yield is denoted by x .

In the limit of small l_e , PY can be calculated analytically. We first calculate PY in the case of a monoenergetic injection of electrons. If we write $n \approx (R/c)\dot{n}$, use the approximation $\dot{n}_0 = (c/R)n_0 \delta(x - x_s)$, neglect higher order scatterings in equations (7) and (9) so that $n(x) = n_0 \delta(x - x_s)$ in the integrands, assume $Q(\gamma) = Q_0 \delta(\gamma - \gamma_{\text{max}})$, neglect P compared to Q in equation (6), and neglect \dot{n}_A , \dot{n}_c^{T} , τ_c , and $\tau_{\gamma\gamma}$, then equation (3) can be solved to give (see ZL85)

$$n(x) = \frac{3^{1/2}}{4} \frac{Q_0 R}{c} x^{-3/2} x_s^{-1/2}, \quad x_s < x < x_{\text{max},1},$$

where

$$x_{\text{max},1} \equiv \frac{4}{3} \gamma_{\text{max}}^2 x_s. \quad (15b)$$

This is the solution for $n(x)$ when electrons are injected monoenergetically, the soft photon source is strong enough so that secondary scatterings can be neglected ($l_s/l_e \gtrsim 0.1$), and pairs can be treated as a perturbation on $n(x)$ ($\text{PY} \ll 1$).

Substituting equation (15a) into equations (11), (13), (14) and using equation (2a), the pair yield in the low compactness limit can be written as

$$\text{PY}(\text{mono}) = \frac{0.3}{4\pi} \frac{l_e}{x_{\text{max},1}} \ln(x_{\text{max},1}). \quad (16)$$

This equation differs by a factor of 2 from the analogous equation (4.28) in S87 due to a different treatment of radiative treatment in that paper (see § IIe[ii] above).

For a power-law injection of electrons with injection index Γ , the results are approximately the same in equations (15) and (16) for $\Gamma < 1$. For $1 < \Gamma < 2$, the pair yield is given by

$$\frac{\text{PY}(1 < \Gamma < 2)}{\text{PY}(\text{mono})} = \frac{(2 - \Gamma)^2}{(\Gamma - 1)^2} (x_{\text{max},1})^{\Gamma-1}, \quad (17a)$$

and for $\Gamma > 2$ the pair yield is given by

$$\frac{\text{PY}(\Gamma > 2)}{\text{PY}(\text{mono})} = (\Gamma - 2)^2 4^{\Gamma-2} 3^{2-\Gamma} x_s^{\Gamma-2} x_{\text{max},1}. \quad (17b)$$

Note that for power-law electron injection, the pair yield can be even higher than that for monoenergetic injection. This is because the pair yield scales as the number of electrons injected, which, for fixed total injected energy, is greater when the injected distribution extends to lower Lorentz factors. The pair yield $\text{PY}(\Gamma)$, for fixed $x_{\text{max},1}$ and x_s , is largest for $\Gamma = 2$.

iv) Pair Annihilation

As mentioned before, we assume that pairs cool down to subrelativistic energies and thermalize before annihilating. If the number densities of these cool thermal positrons and electrons are n_+ and n_- , respectively, then the rate of pair annihilation may be written as (see S87; Svensson 1982)

$$\frac{dn_+}{dt} = -\frac{3}{8} g_a(\Theta) \sigma_T c n_+ n_- = -\frac{1}{2} \int_1^{\gamma_{\text{max}}/2} P(\gamma) d\gamma, \quad (18a)$$

$$g_a = [1 + 2\Theta^2 / \ln(1.12\Theta + 1.3)]^{-1}. \quad (18b)$$

The second equality in equation (18a) expresses the require-

ment that, for a plasma at rest, positrons must be destroyed at the same rate they are created, in steady state. When the plasma is in motion, for example flowing toward a black hole, steady state requires that the creation rate of positrons be balanced by the *sum* of the annihilation rate and the inflow rate (see Lightman, Zdziarski, and Rees 1987; Begelman, Sikora, and Rees 1987). Unless otherwise specified, we will assume in this paper that the plasma is at rest.

For the pair annihilation spectrum, we use the spectral fit of Svensson (1983). For $\Theta \ll 1$, the spectrum becomes

$$\dot{n}_A(z) = \frac{1}{g_a \pi^{1/2}} \left[\int P(\gamma) d\gamma \right] \Theta^{-1/2} x^{3/2} \exp \left[\frac{-(x-1)^2}{x\Theta} \right]. \quad (19)$$

Determination of the temperature Θ and of the broadening of the annihilation line due to thermal scattering will be discussed in § IIg below.

v) Scattering Depth to Thermal Pairs

The Thomson scattering depth to thermal pairs is

$$\tau_T = R \sigma_T (n_+ + n_-). \quad (20a)$$

Using $n_+ = n_-$, equations (2a), (14), and (18), equation (20a) may be written as (see Guilbert, Fabian, and Rees 1983),

$$\tau_T = \left(\frac{4}{\pi g_a} l_e P Y \right)^{1/2}. \quad (20b)$$

In determining τ_T , we have neglected the cooled primary electrons, assuming that an effective reacceleration occurs.

f) Photon Escape

Photons not absorbed are impeded from escaping in a time $\sim R/c$ by scattering. Scattering by (high-energy) nonthermal electrons drastically changes the energy of a photon and is treated as absorption. In this section, therefore, we consider scattering only by the (low-energy) thermal electrons.

Spatial diffusion is modeled by a mean interior photon density $n(x)$ and an escape rate \dot{n}_{esc} . We approximate the photon escape rate as

$$\dot{n}_{\text{esc}} = \frac{c}{R} n(x) \left[1 + \frac{1}{3} \tau_{\text{KN}} f(x) \right]^{-1}, \quad (21a)$$

where

$$f(x) = \begin{cases} 1, & x \leq 0.1, \\ (1-x)/0.9, & 0.1 < x < 1, \\ 0, & x \geq 1, \end{cases} \quad (21b)$$

and

$$\tau_{\text{KN}}(x) = \tau_T \sigma_{\text{KN}}(x) / \sigma_T. \quad (21c)$$

Here $\sigma_{\text{KN}}(x)$ is the Klein-Nishina cross section (see, e.g., Jauch and Rohrlich 1980, eq. [11.24]). In the nonrelativistic regime, $x < 0.1$ and $f(x) = 1$, this expression approximates the results of equations (8) and (9) in Sunyaev and Titarchuk (1980) for the case of photon sources distributed sinusoidally throughout a spherical volume. For this special distribution, which is not far from a uniform distribution, equation (3) is a good approximation to the spatial diffusion problem.

In the relativistic regime, $x \gtrsim 1$, the large energy shift in a single scattering effectively removes a photon of energy x from $n(x)$ upon scattering. In addition, forward scattering becomes more important. Thus, at each energy x a diffusive buildup of photons in the interior cannot occur. A photon either scatters and reappears at a new x , as included in \dot{n}_C^T and treated below, or it escapes in a time R/c . The $f(x)$ function smoothly makes this transition from the nonrelativistic to the relativistic regimes. We determined $f(x)$ by comparing the solution of equation (3), without pair processes, to the results of Monte Carlo calculations, injecting photons of energies $10^{-4} \lesssim x \lesssim 10^2$ into a sphere of scattering depths τ_T ranging from 3 to 12 (Lightman and Zdziarski 1987). The function $f(x)$ was the simplest one that gave a good fit to the Monte Carlo results. (We point out, however, that the choice of $f[x]$ depends somewhat on the adopted relativistic corrections to the Kompaneets equation; see § IIg[i] and Lightman and Zdziarski 1987.) Earlier calculations (FBGPC86; S87) did not include relativistic modifications to the escape rate for energies $x \lesssim 1$.

g) Thermal Compton Scattering

i) Scattering the Continuum

For $x \leq 1$, we use the Kompaneets equation, with an empirical modification by Cooper (1971), to describe thermal Comptonization off thermal electrons of temperature Θ and scattering depth τ_T :

$$\dot{n}_C^T = \frac{c}{R} \tau_T \frac{d}{dx} \left[\omega(x) x^4 \left(\Theta \frac{du}{dx} + u \right) \right], \quad (22a)$$

where

$$u \equiv n/x^2 \quad (22b)$$

is proportional to the photon occupation number and

$$\omega(x) = (1 + 4.6 + 1.1x^2)^{-1} \quad (22c)$$

is a fit to the relativistic corrections to the mean photon energy shift for scattering on cold electrons, allowing equation (22a) to be used up to energies $x \sim 1$ in the limit of $\Theta \ll 1$ (Cooper 1971). The stimulated emission term in the Kompaneets equation has been dropped. Dispersion in the final energies of photons with $x \gtrsim \Theta$ has been neglected. This dispersion is much less important for scattering the continuum (as in our problem) than for scattering lines (see Ross, Weaver, and McCray 1978). Equation (22), as many of our other equations, must be solved numerically.

For $x \gtrsim 1$, equation (22) is no longer an accurate description of the scattering process. However, there are relatively few photons in this region, and, when scattered, they appear at much lower energies $x < 1$. Thus, it is a good approximation simply to remove these photons in proportion to their probability for scattering and to neglect their reappearance at low energies. Accordingly, for $x > 1$, we take

$$\dot{n}_C^T = -\frac{c}{R} n(x) \tau_{\text{KN}}(x). \quad (23)$$

Equations (21), (22), and (23) give results that are in good agreement with detailed Monte Carlo calculations over a wide range of values of Θ and τ_T (see Lightman and Zdziarski 1987 for further discussion).

S87 treated thermal Comptonization as in equation (23) for $x \geq 1$ and, for $x < 1$, took Comptonization into account

by multiplying injected photon spectra by the factor $\{1 - \exp[-(3/x\tau_T^2)^{1/2}]\}$. This approximation assumes $\Theta = 0$ and so cannot treat the upscattering of X-rays by thermal electrons. Thermal upscattering of the input soft photons in S87 is treated using the actual Θ . FBGPC86 shifted photon energies by $\Delta x/x = 4\Theta - x/(1+x)$ on each scattering, neglecting the dispersion $\langle(\Delta x)^2\rangle$, and used the Thomson cross section at all energies. For large τ_T , relativistic modifications to the escape probabilities and to the Kompaneets equation lower the effective value of τ_T significantly and cause substantial differences between our results and those of S87 and FBGPC86 in the region $1/\tau_T^2 \lesssim x \lesssim 1$. This is further discussed in § IV.

ii) Scattering, Absorption, and Escape of the Annihilation line

When $\Theta \ll 1$, the narrow annihilation line is not accurately treated by equation (22), which approximates discrete scattering by a continuous change of the photon energy. However, we can use some approximations to find an analytic solution to the scattering of the line and can treat the escaping photons separately. The total rate of production of photons in the annihilation line is

$$\int \dot{n}_A(x) dx = \int_1^{\gamma_{\max}^2} P(\gamma) d\gamma. \quad (24)$$

Of this, a fraction $f_e = 1/(1 + \tau_{KN} + \tau_C^{\text{NT}} + \tau_{\gamma\gamma})$ escapes without scattering or absorption and emerges with the distribution $f_e \dot{n}_A(x)$ (see eq. [19]), and a fraction $(1 - f_e)$ is either downscattered or absorbed before escaping. (Here scattering by non-thermal electrons is treated as absorption, and f_e should be evaluated at $x = 1$.) We treat the second fraction now.

For $\Theta \ll 1$ and $x \approx 1$, the Θ term in equation (22a) may be neglected. As further approximations, we set $x = \frac{1}{2}$ in $f(x)$ (eq. [21b]), in $\omega(x)$ (eq. [22c]), and in τ_C^{NT} and $\tau_{\gamma\gamma}$, since x does not vary much over the downscattered line. We approximate the source of line radiation as proportional to a δ -function at $x = 1$. Then, equation (3), applied only to the line emission, reads

$$\frac{d}{dx} (x^2 n) + S\delta(x-1) - \xi n = 0, \quad (25a)$$

where

$$S \equiv \frac{R(1-f_e) \int P(\gamma) d\gamma}{c \tau_T \omega}, \quad (25b)$$

$$\xi \equiv \frac{1}{\tau_T \omega} \left(\tau_C^{\text{NT}} + \tau_{\gamma\gamma} + \frac{1}{1 + (1/3)\tau_{KN} f} \right), \quad (25c)$$

and ω , τ_C , $\tau_{\gamma\gamma}$, and f are to be evaluated at $x = \frac{1}{2}$, as discussed above. The dominant contributions to f_e and ξ come from τ_{KN} . The solution to equation (25) for the downscattered annihilation line is

$$n(x) = \frac{1}{x^2} S e^{-\xi(1/x-1)}, \quad x \leq 1, \quad (26)$$

and $n(x) = 0$ for $x > 1$ (see Sunyaev and Titarchuk 1980). The photon density given by equation (26) is then added to the solution of $n(x)$ for the continuum.

iii) Determination of the Thermal Temperature

The equilibrium temperature of the thermal electrons and positrons is determined by requiring that no net energy be

transferred between particles and photons:

$$\int \dot{n}_C^T x dx = 0. \quad (27)$$

Using equations (22) and (23), performing two integrations by parts, and neglecting the $\Theta du/dx$ term compared to the u term at $x = 1$, equation (27) yields for the equilibrium temperature:

$$\Theta = \frac{\int_0^1 \omega x^2 n dx - \omega(1)n(1) + \int_1^\infty x n \sigma_{KN} dx}{4 \int_0^1 \omega x n dx + \int_0^1 x^2 (d\omega/dx) n dx - \omega(1)n(1)}. \quad (28)$$

When the photon density does not extend up to the relativistic domain, i.e., $n(x) = 0$ for $x \gtrsim 0.1$ and $\omega = 1$, only the first terms in the denominator and numerator of equation (28) are nonzero and our expression reduces to the usual expression for the "Compton temperature," e.g., equation (4) in Guilbert, Fabian, and Rees (1983). For relativistic photon energies, the additional terms are important. Recently, Guilbert (1986) has derived an integral for the equilibrium temperature without assuming validity of the Kompaneets equation.

III. THE PAIR-REDUCED EDDINGTON LIMIT AND THE PAIR RATIO

a) The Pair-reduced Eddington Limit, L_E^* , and the Pair Ratio, $2n_+/n_i$, for Accretion onto a Black Hole

In this section, we assume that the electron-positron pairs are produced within a gas that is accreting onto a central black hole of mass M . As before, we assume that the pairs are prevented from escaping. Such trapping of pairs may arise either from magnetic fields or from collective plasma effects. It is plausible that the pairs will then be coupled to the protons and can transmit radiation pressure to them. Since each proton is thus effectively coupled to $1 + 2n_+/n_i$ electrons, where n_+ and n_i are the positron and proton densities, respectively, the Eddington limit is reduced to the value

$$L_E^* = \frac{L_E}{1 + 2n_+/n_i}. \quad (29)$$

The pair-reduced Eddington limit, L_E^* , is the maximum possible luminosity in steady state, at which point the inward gravitational force on each proton is balanced by the outward radiation force on the $(1 + 2n_+/n_i)$ electrons attached to it.

When the luminosity L is generated by gravitational energy, n_i may be calculated in terms of L . The rate of matter inflow can be written as $\dot{M} = 4\pi R^2 \rho v_r$, where $\rho = m_p n_i$ is the matter density and v_r is the inward radial velocity. Setting $v_r = (2GM/R)^{1/2}/\mu$, where $(2GM/R)^{1/2}$ is the free-fall velocity and $\mu \geq 1$ measures the departure from free fall, defining the efficiency of accretion $\epsilon \equiv L/\dot{M}c^2$, writing $L = (Rm_e c^3/\sigma_T) l_e (1 + l_s/l_e)$, and using equation (20b) with $g_a = 1$, we obtain for the pair ratio

$$\frac{2n_+}{n_i} = 0.9 \left(\frac{m_p}{m_e} \right) \left(\frac{PY}{l_e} \right)^{1/2} \frac{1}{1 + l_s/l_e} \frac{\epsilon_{0.1}}{\mu} \left(\frac{2R_S}{R} \right)^{1/2}, \quad (30)$$

valid for $2n_+ \gg n_i$. Here $\epsilon_{0.1} \equiv \epsilon/0.1$. In using equation (20b) in the derivation of equation (30), we have assumed that pair annihilation dominates pair inflow. As is shown by Lightman, Zdziarski, and Rees (1987), this is always valid for $l_e \gtrsim 10^2$. Unless the scattering depth is sufficiently large to trap the outgoing radiation (see discussion below), we expect $\epsilon_{0.1} \approx 1$. Furthermore, we assume that energy is liberated down to a radius $R \approx 2R_S$ for accretion onto a black hole. For spherical

accretion at the free-fall velocity, $\mu = 1$. For disk accretion, μ can substantially exceed unity, and $2n_+/n_i$ is accordingly reduced. In our detailed calculations, we take $\mu = 2$, corresponding to nearly spherical accretion with some slowing due to angular momentum and dissipative drag. As can be seen from equation (30), the pair ratio $2n_+/n_i$ may greatly exceed unity for nonthermal production of pairs, in contrast to thermal production (e.g., Schultz and Price 1985). At $l_e = 100$, for example, where $PY \approx 0.1$, $2n_+/n_i \approx 25$ for $\epsilon_{0.1} = 1$, $\mu = 2$, $R = 2R_S$, and $l_s/l_e \approx 0$.

Using equation (1b) with $l = l_e + l_s$, the luminosity as a function of the pair-reduced Eddington limit is

$$\frac{L}{L_E^*} = \frac{L}{L_E} \frac{L_E}{L_E^*} = \frac{m_e}{m_p} \left(\frac{1}{\pi} \right) l_e \left(1 + \frac{l_s}{l_e} \right) \left(\frac{R}{2R_S} \right) \left(1 + \frac{2n_+}{n_i} \right), \quad (31)$$

where $2n_+/n_i$ is given by equation (30).

b) Compactness and Pair Ratio at the Maximum Luminosity

Unlike the classical Eddington limit L_E , which depends only on M , the pair-reduced Eddington limit L_E^* depends on many different parameters. However, this dependence simplifies near the maximum luminosity, $L = L_E^*$. When $L = L_E^*$, equations (30) and (31) can be solved together for l_e , giving, for $2n_+/n_i \gg 1$,

$$l_e \approx 130 \left(\frac{PY}{0.1} \right)^{-1} \left(\frac{\mu}{\epsilon_{0.1}} \right)^2 \left(\frac{2R_S}{R} \right). \quad (32)$$

For values of $l_e \gtrsim 50$, $PY \approx 0.1$ independent of γ_{\max} , l_s/l_e , Γ , and x_s . Taking $PY = 0.1$, equations (29), (30), and (32) give

$$\frac{L_E}{L_E^*} \approx \frac{50}{(1 + l_s/l_e)} \left(\frac{\epsilon_{0.1}}{\mu} \right)^2 \quad (33)$$

at the maximum luminosity, $L = L_E^*$. Thus, for small values of l_s/l_e and $\mu \approx 1-2$, the creation of pairs may limit the maximum luminosity to a factor ~ 10 below the classical Eddington limit.

The above analysis ignores radiation trapping by the infalling matter. This effect becomes important when the scattering depth closest to the black hole (where most of the luminosity is produced) satisfies $\tau_T v_r/c > 1$ (e.g., Begelman 1979) and causes the accretion efficiency to decrease with increasing \dot{M} . When such effects are included (Lightman, Zdziarski, and Rees 1987), it is found that L/L_E^* never actually reaches unity, but increases with \dot{M} until it reaches a value of ~ 0.5 and remains constant at this value for higher \dot{M} . Equation (33) provides a good estimate for L_E/L_E^* at the lowest value of \dot{M} for which L/L_E^* has reached its maximum value of ~ 0.5 , at an l_e given approximately by equation (32). This is also the point where radiation trapping first becomes important. It seems plausible that when $L/L_E^* \approx 0.5$ globally, inhomogeneities in the spherical flow or in the energy production rate may create local regions where $L/L_E^* > 1$, leading to outward flows and modifications in the accretion rate. In this way, the maximum steady luminosity might still be limited to a factor of ~ 10 below the classical Eddington limit, as mentioned above. Dynamical calculations are needed to explore these effects.

We point out that the pair-reduced Eddington limit described above differs from the pair-induced luminosity limit cycles recently proposed by Moskalik and Sikora (1986) and discussed further by Wandel and Mushotzky (1986). Moskalik and Sikora assume that thermal protons store up a large amount of energy, which is suddenly transferred to thermal

pairs when the latter's number density reaches a critical point. Depending on parameters, this instability happens at a luminosity $L/L_E \sim 10^{-2}$ and leads to a time-dependent limit cycle about this value of luminosity. For higher or lower values of L , such an instability does not occur. In contrast, the effect we consider derives from the opacity of the pairs, which might have dynamical consequences at a luminosity $L = L_E^* \sim 0.1L_E$.

IV. NUMERICAL RESULTS

Emergent spectra are shown in Figures 1–7, and in Figure 9 for a number of different models. The emergent spectrum is given in the units $dl(x)/d \ln x = x^2 \dot{n}_{\text{esc}}(x)(4\pi R^2 \sigma_T/3c)$. In Figures 1, 2, 6, and 9, the (narrow) width of the unscattered annihilation line has been set to zero. To allow visibility, the unscattered annihilation lines have been removed in the $l_e = 100$ curves in Figures 1 and 2. For most models, an annihilation feature is visible for $l_e \gtrsim 10$ even neglecting the unscattered annihilation line, which could be eliminated by macroturbulence and bulk motion of the gas.

a) Effects of Thermal Electrons

For $\tau_T > 1$, a significant depletion of the spectrum is visible in the region $1/\tau_T^2 \lesssim x \lesssim 1$, due to downscattering of photons by cold thermal electrons (see Sunyaev and Titarchuk 1980). This depletion lessens in the region $0.1 < x < 1$ due to the relativistic corrections $\omega(x)$ in equation (22c) and $f(x)$ in equation (21b), which decrease the effective value of τ_T . As a result, the depletion from downscattering is maximal at $x \approx 0.1$. With this depletion, there is a corresponding increase of photons in the region $1 < x < \tau_T^2$, because such photons have fewer photons at energies $1/x$ to absorb them in pair production. The higher l_e curves demonstrate these effects. Another effect of thermal Comptonization at large τ_T is the upscattering of low-energy photons. For smaller values of l_s/l_e (e.g. Fig. 2 for high l_e) the equilibrium temperature is necessarily larger and the upscattering of the soft component of the spectrum can be very significant (see Figs. 1 and 2). We point out that the Compton y parameter, $y \equiv 4\tau_T(1 + \tau_T/3)$ in our approximation to radiative transfer, never reaches unity in our models, so that the resulting spectra never show features at energies corresponding to the temperatures of the thermal pairs, in contrast to the earlier estimates of Guilbert, Fabian, and Rees (1983).

b) First-Order Scattering by Nonthermal Pairs

This effect is due to scattering of the primary photons by the part of the electron distribution, $N(\gamma)$, proportional to $\int P(\gamma)$ (see eq. [6]) and has been discussed in detail by Kazanas (1984), ZL85, and S87. In order for the scattering of the primary photons to dominate over higher order scatterings, $l_s \gtrsim l_e$ is required. A more accurate criterion for higher order Compton scatterings to be unimportant is that the first-order scattering spectrum, including scattering by pairs, intersects the blackbody spectrum much below its peak. For a power-law spectrum extending to some break energy x_b with a mean spectral index $\langle \alpha \rangle$, this condition can be written in an approximate manner as

$$\frac{l_s}{l_e} \gg \begin{cases} (x_s/x_b)^{1-\langle \alpha \rangle} & \langle \alpha \rangle < 1; \\ 1, & \langle \alpha \rangle \gtrsim 1. \end{cases} \quad (34)$$

The spectral component produced by scattering by pairs has an index at $x \ll 1$ that is always less than unity (S87). Therefore, the spectrum formed by scattering by the pairs will be

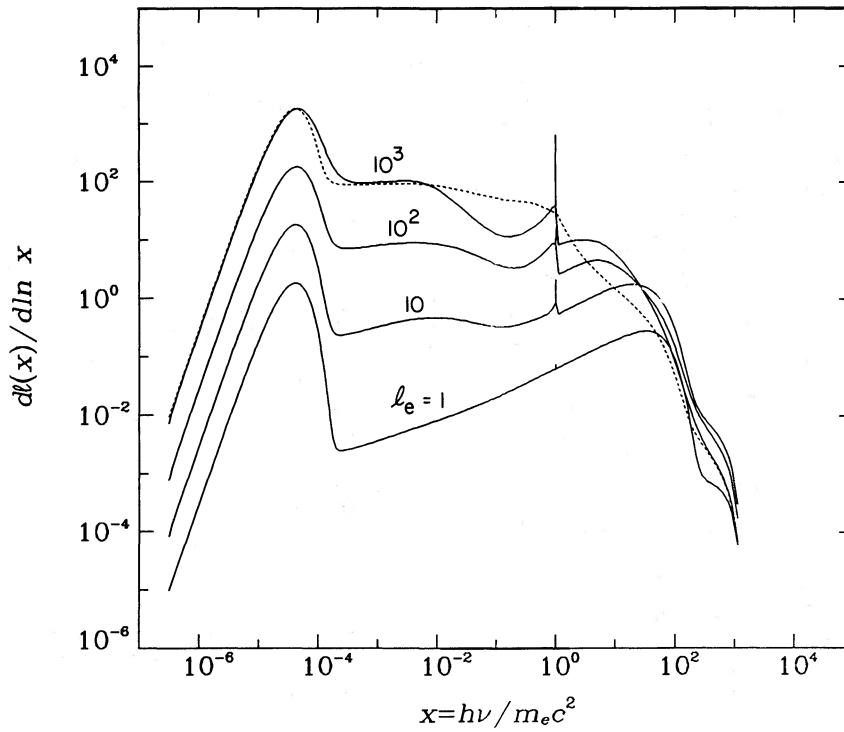


FIG. 1.—Emerging spectra for a blackbody photon injection at peak energy x_s , and a monoenergetic electron injection at Lorentz factor γ_{\max} , under the combined processes of Compton scattering, pair production, and photon escape. For these models, $\gamma_{\max} = 1.2 \times 10^3$, $x_s = 3 \times 10^{-5}$, and $l_s/l_e = 2.5$, where l_s/l_e is the ratio of soft photon compactness parameter l_s to electron compactness parameter l_e . Dotted curve is the $l_e = 10^3$ model without thermal Comptonization included. For clarity, the unscattered annihilation line has been omitted from the $l_e = 100$ model. Note the effect of downscattering on the annihilation line for high l_e . The high-energy break in the $l_e = 10^2$ and 10^3 spectra at $x \approx 10$ is caused by pair production. Parameters of the $l_e = 10$ and 100 curves are given in Table 1, models F and G.

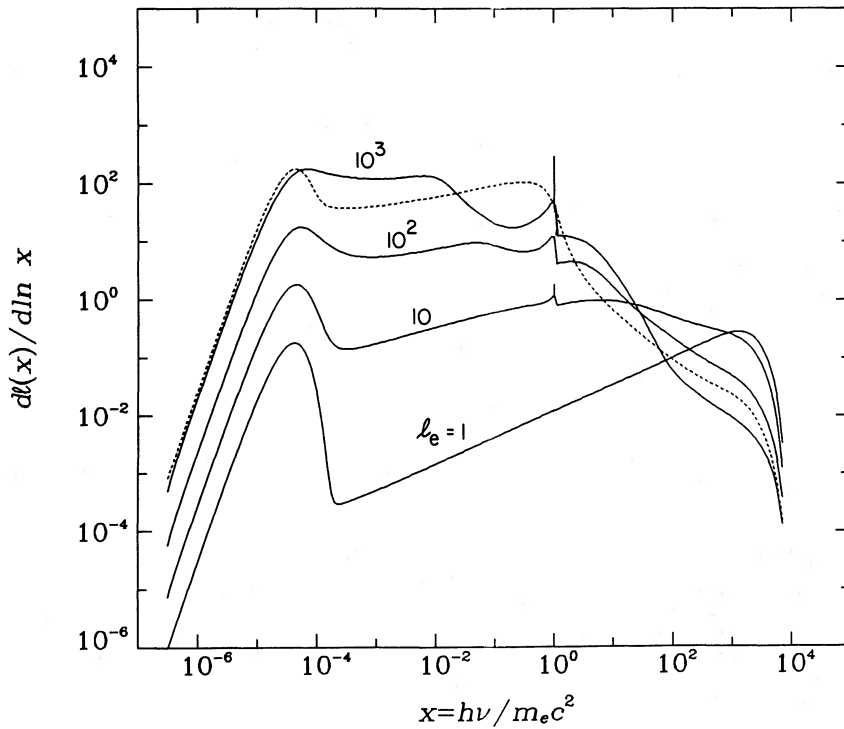


FIG. 2.—Same as in Fig. 1, but with $\gamma_{\max} = 7.5 \times 10^3$ and $l_s/l_e = 0.25$. For the $l_e = 1000$ model, $\tau_T = 15$. Note the large depletion of photons in the region $1/\tau_T^2 \leq x \leq 1$, caused by downscattering by thermal pairs at low energies, $\Theta = 2 \times 10^{-3}$. Note also the upscattering of the input blackbody photons by these same pairs. See Table 1, models A, B, D, E, for the model parameters.

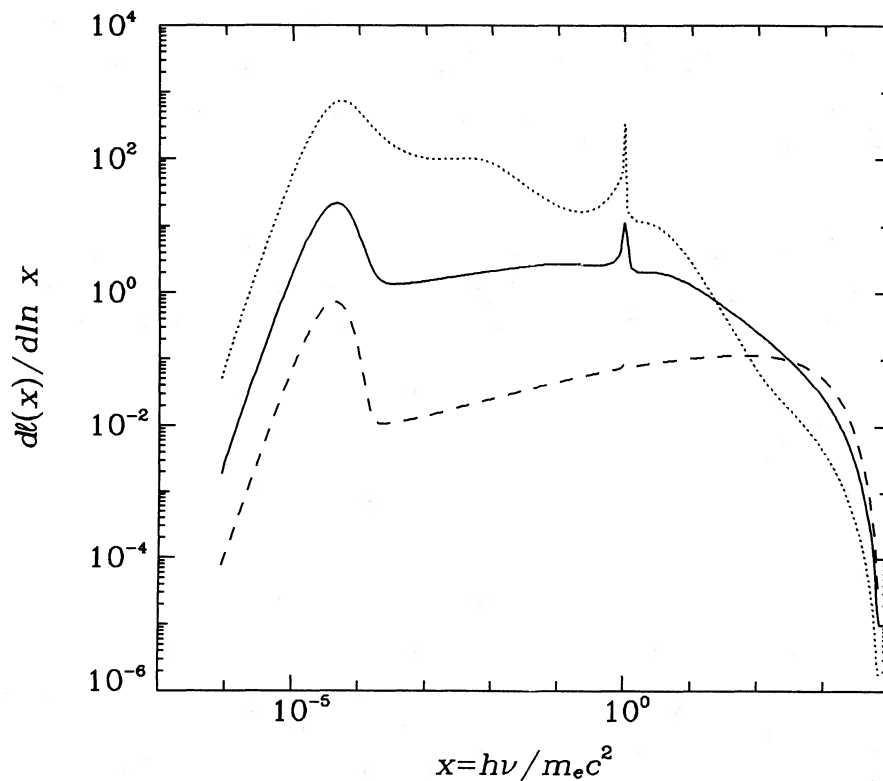


FIG. 3.—Emerging spectra for power-law primary electron injections at $\gamma_{\min} \leq \gamma \leq \gamma_{\max}$, $\gamma_{\min} = 1$ (for this and all power-law models below), $\gamma_{\max} = 7.5 \times 10^3$, $\Gamma = 1.5$, $x_s = 3 \times 10^{-5}$, and $l_s/l_e = 1$. Dashed, solid, and dotted curves are for $l_e = 1, 30$, and 1000 , respectively. See Table 2, models a, b, c.

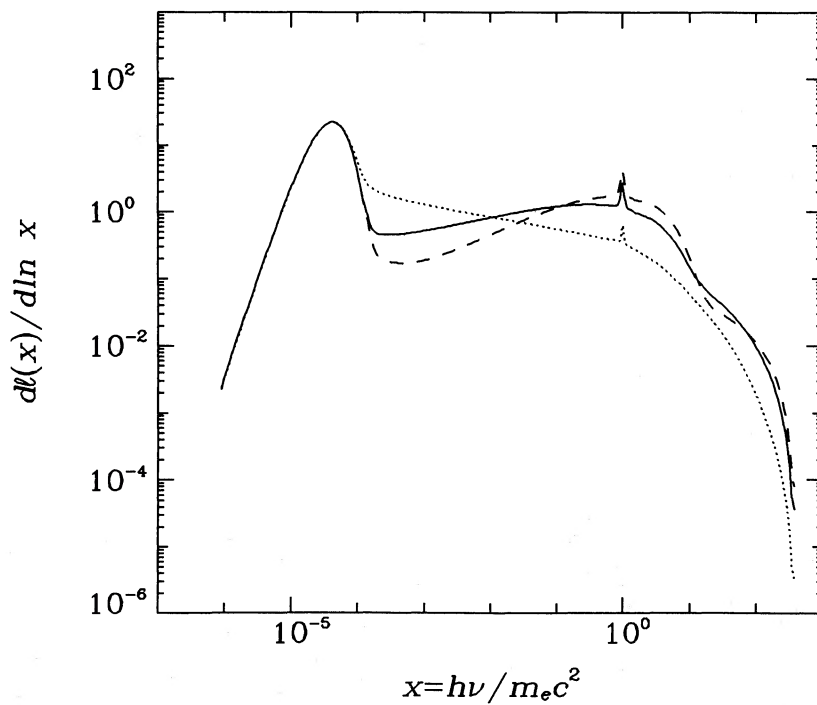


FIG. 4.—Emerging spectra for power-law primary electron injections, showing the effect of varying the injection index Γ at fixed electron and soft photon compactnesses. Dashed, solid, and dotted curves are for $\Gamma = 0.5, 1.5$, and 2.5 , respectively. For all models, $l_e = 10$, $l_s/l_e = 3$, $\gamma_{\max} = 400$, and $x_s = 3 \times 10^{-5}$. The high-energy break in the spectra at $x \lesssim 10$ is caused by the low value of γ_{\max} , not by pair production. See Table 2, models d, e, and f.

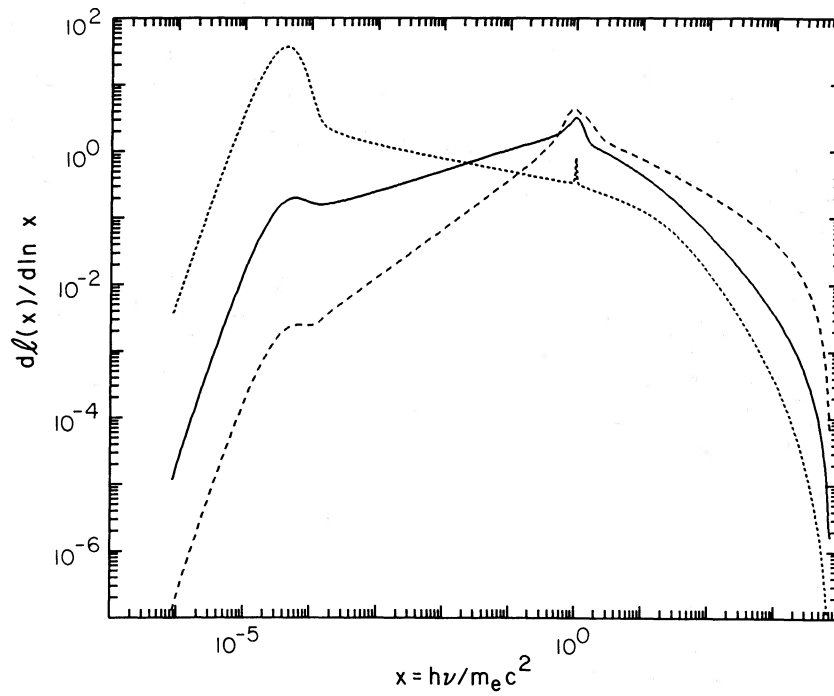


FIG. 5.—Emerging spectra for power-law primary electron injections, showing the effect of varying the ratio of soft photon compactness to electron compactness, l_s/l_e , at fixed electron compactness and fixed injection index. Dashed, solid, and dotted curves are for $l_s/l_e = 10^{-3}$, 3×10^{-2} , and 5, respectively. For all models $\Gamma = 2.5$, $\gamma_{\max} = 7.5 \times 10^3$, and the values of l_e and x_e are the same as in Fig. 4. The high-energy break in the low l_s/l_e spectra at $x = 1$ is caused by the dominance of high-order scatterings and reduction of the Klein-Nishina cross section, not by pair absorption. See Table 2, models g, h, and i.

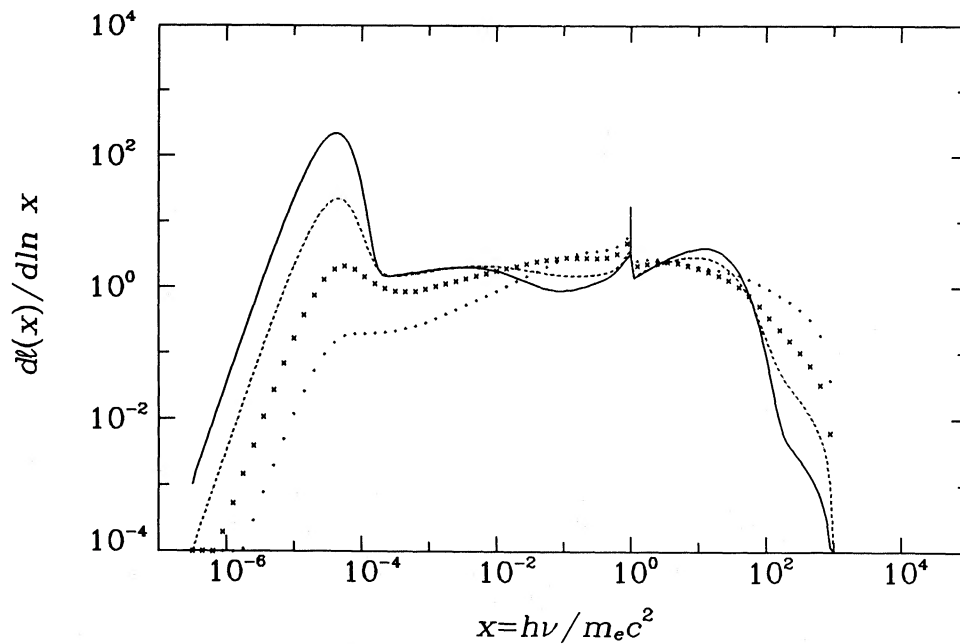


FIG. 6.—Emerging spectra for $x_e = 3 \times 10^{-5}$, $\gamma_{\max} = 10^3$, and $l_e = 30$, showing the effect of varying l_s/l_e for monoenergetic electron injections. Dotted, crossed, dashed, and solid curves represent $l_s/l_e = 0.01$, 0.1, 1, and 10, respectively. The dip in the spectra of the high l_s/l_e curves at $x \gtrsim 0.01$ is caused by the decrease in photon production by injected pairs, not by Comptonization. Note the broad shoulders extending to energies beyond $x_{\max, 1} = (4/3)\gamma_{\max}^2 x_e = 40$, especially in the low l_s/l_e curves. These shoulders are caused by higher order Compton scattering. See Table 1, models N, O, P.

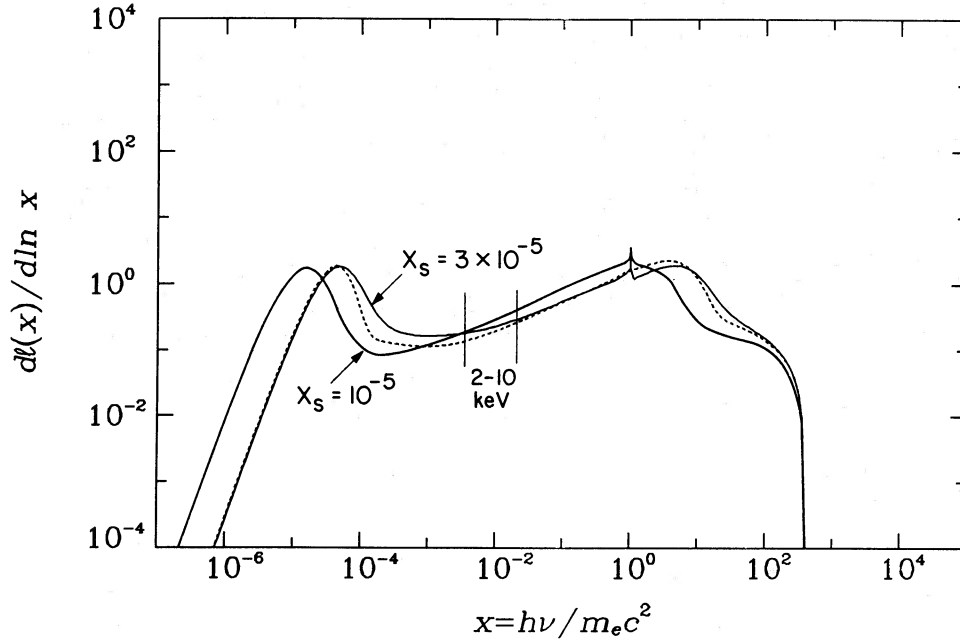


FIG. 7.—Emerging spectra for monoenergetic injections at $\gamma_{\max} = 400$, $l_e = 10$, and $l_s/l_e = 0.25$, showing the effect of varying x_s . Dotted curve is the $x_s = 3 \times 10^{-5}$ model without thermal Comptonization included. Vertical lines show the 2–10 keV X-ray energy range. See Table 1, models L and M.

most visible for the smallest possible spectral index from the scattering by the primary electrons. The latter index is $\alpha = \Gamma/2$ for $\Gamma > 1$ and $\alpha = 0.5$ for $\Gamma \leq 1$ (which includes the case of monoenergetic injection). For $\Gamma > 2$, the contribution of pairs to the spectrum will be invisible.

For $l_e \gg 1$, the X-ray spectral index, α , approaches a maximum value that depends on the number of pair generations (S87). If $x_{\max,2} < 1$ (see eq. [35]), there is only one pair generation. If $x_{\max,2} > 1$, relation (35) can be applied recurrently to find the last $x_{\max,k}$ which is still greater than 1, giving k generations.

Figure 1 presents examples with monoenergetic injection at $\gamma_{\max} = 1200$ and $x_s = 3 \times 10^{-5}$, which give only one pair generation. For $l_e = 1$ and 10, the thermal downscattering is negligible; for $l_e = 10^3$, the dotted curve shows the un-Comptonized spectrum. Figure 2 shows cases with $\gamma_{\max} = 7500$, $x_{\max,2} \sim 10^2$, and two pair generations. The $x \ll 1$ nonthermal slopes for $l_e = 10^2$ and 10^3 are $\alpha \approx 0.8$ –1.

For lower l_e , the spectral indices at $x \ll 1$ increase from $\alpha = 0.5$ for $l_e \ll 1$ to the asymptotic values given above and in S87. This effect is seen in Figures 1 and 2.

For *power-law* primary electron injections with $\Gamma < 2$, the effect of nonthermal first-order scattering by pairs increases the X-ray index from $\alpha = \Gamma/2$ (in the absence of pairs, $l_e \ll 1$) to $\alpha \leq 1$ for $l_e \gg 1$. This is illustrated in Figure 3.

Another feature visible in some spectra is a dip at energies $x \gtrsim x_{\max,2}$, where

$$x_{\max,2} \equiv \frac{16}{27} x_s^3 \gamma_{\max}^4 \quad (35)$$

is the maximum energy of photons created by the first generation of pairs when first-order scattering dominates (ZL85; S87). The spectrum falls at energies $x > x_{\max,2}$, because the photons produced by pairs no longer contribute, but it eventually rises again from the photons produced by primary electrons. When $x_{\max,2}$ lies in the range $10^{-2} \lesssim x_{\max,2} \lesssim 1$, this

“secondary injection” effect has some of the appearances of depletion by Compton downscattering. In the models in Figure 1, for example, $x_{\max,2} = 3 \times 10^{-2}$. The $l_e = 10$ curve shows a dip above $x_{\max,2}$. However, τ_T is only 0.59 (model F in Table 1), not large enough to produce this apparent depletion. It is caused rather by the secondary injection effect. By comparison, for the $l_e = 10$ curve in Figure 2, $x_{\max,2} = 45$, and a dip does not occur at $x < 1$. When $l_s/l_e \ll 1$, the relative importance of higher order scatterings tends to wash out the dip at $x \gtrsim x_{\max,2}$. For example, in Figure 6, $x_{\max,2} = 1.6 \times 10^{-2}$ and τ_T ranges from 1.5 to 2.4 (models N, O, P in Table 1). A dip at $x \gtrsim x_{\max,2}$ is visible for $l_s/l_e = 1$ and 10 and is absent for $l_s/l_e = 10^{-2}$ and 10^{-1} .

c) Higher Order Scatterings by Nonthermal Particles

When inequality (34) is satisfied, the resulting spectrum is completely insensitive to the l_s/l_e ratio (see ZL85), except for the width of the annihilation line, determined by the Compton temperature. When l_s/l_e decreases, higher order Compton scattering by nonthermal electrons and pairs become important, and the value of l_s/l_e becomes critical to the spectrum. This case has been studied analytically by Zdziarski and Lamb (1986) for power-law injections with $\Gamma > 1 + \alpha$. For $l_s/l_e \ll 1$, the spectrum must rise steeply at low x to produce the required luminosity, and α is small. The index α then increases with increasing l_s/l_e . There is a break at $x = 1$ (see § IVd), and, in the absence of pair absorption, the $x > 1$ spectral index is $\alpha_y \approx \Gamma - 1$ (see Fig. 5). Compton scattering by nonthermal pairs does not modify these indices.

Figure 6 demonstrates the effect of decreasing l_s/l_e for monoenergetic electron injection. Similarly as in Figure 5, α decreases with decreasing l_s/l_e . Note also in Figure 6 that α is affected by secondary pair injection for high l_s/l_e , but not for low l_s/l_e , where higher order scatterings dominate and smooth out the spectrum.

TABLE 1
RESULTS FOR SELECTED MODELS WITH MONOENERGETIC ELECTRON INJECTION

l_e	l_s/l_e	x_s	γ_{\max}	τ_T	θ	PY	l_s/l_e	α	x_*	Model
1.....	0.25	3×10^{-5}	7.5×10^3	1.2×10^{-2}	2.2×10^{-2}	1.1×10^{-4}	2.3×10^{-3}	0.53	7.5×10^3	A
10.....	0.25	3×10^{-5}	7.5×10^3	0.66	3.1×10^{-2}	3.4×10^{-2}	5.8×10^{-2}	0.73	36	B
30.....	0.25	3×10^{-5}	7.5×10^3	1.63	1.9×10^{-2}	7.0×10^{-2}	9.0×10^{-2}	0.79	6.0	C
100.....	0.25	3×10^{-5}	7.5×10^3	4.4	8.8×10^{-3}	0.15	0.13	0.81	1.7	D
1000.....	0.25	3×10^{-5}	7.5×10^3	15	2.0×10^{-3}	0.18	0.22	1.4	1	E
10.....	2.5	3×10^{-5}	1.2×10^3	0.59	5.6×10^{-3}	2.7×10^{-2}	8.5×10^{-2}	0.97	35	F
100.....	2.5	3×10^{-5}	1.2×10^3	3.6	1.8×10^{-3}	0.1	0.15	1.08	3.4	G
40.....	1	10^{-4}	1.0×10^3	2.1	6.6×10^{-3}	8.9×10^{-2}	0.13	0.80	4.1	H
400.....	1	10^{-4}	1.0×10^3	8.8	2.0×10^{-3}	0.15	0.17	0.97	1	I
5.....	10	3×10^{-5}	3×10^3	0.32	1.4×10^{-2}	1.6×10^{-2}	7.8×10^{-2}	0.73	65	J
400.....	10	3×10^{-5}	3×10^3	7.2	3.3×10^{-4}	0.10	0.14	0.91	1	K
10.....	0.25	3×10^{-5}	400	0.76	4.2×10^{-2}	4.4×10^{-2}	3.7×10^{-2}	0.72	60	L
10.....	0.25	1×10^{-5}	400	0.83	3.4×10^{-2}	5.3×10^{-2}	4.5×10^{-2}	0.56	31	M
30.....	0.01	3×10^{-5}	1.0×10^3	2.4	5.4×10^{-2}	0.15	4.7×10^{-2}	0.49	3.7	N
30.....	0.1	3×10^{-5}	1.0×10^3	2.1	2.5×10^{-2}	0.11	9.5×10^{-2}	0.73	5.0	O
30.....	10.0	3×10^{-5}	1.0×10^3	1.5	1.1×10^{-3}	5.6×10^{-2}	9.9×10^{-2}	1.20	15	P

d) High-Energy Break

A critical feature of the spectra, especially when comparing to observations, is the high-energy break (or turnover). For scattering models, there are four characteristic energies at which a break can occur, depending on parameters: $x_{\max,1}$, the maximum photon energy from first-order scattering by primary electrons; x_* , the energy above which the optical depth to pair production exceeds unity; 1, the energy below which electrons of Lorentz factor about unity can scatter photons in the Thomson limit; and γ_{\max} , the maximum electron energy. The appropriate conditions for each of these characteristic break energies are discussed below. We point out that, within the context of scattering models, only the break at $x = 1$ (which coincides with $x = x_*$ for $l_e \gtrsim 100$) is independent of the details of the primary injections of soft photons and electrons.

i) Breaks for $l_s/l_e \gg 1$

For $l_s/l_e \gg 1$, first-order scatterings dominate and the high-break occurs at the *minimum* of x_* and $x_{\max,1}$, where x_* is defined by

$$\tau_{\gamma\gamma}(x_*) \equiv 1, \quad (36)$$

and $x_{\max,1}$ is defined in equation (15b). The energy $x_{\max,1}$ is the maximum energy attainable by first-order (single) scatterings of photons at the peak of the injected blackbody distribution, $x = x_s$. The spectrum at energies $x > x_*$, where $\tau_{\gamma\gamma} > 1$, is depleted by absorption of photons in pair production. For increasing l_e , x_* decreases toward unity. As can be seen in the figures and in Table 1, typically $x_* > 10$ for $l_e \lesssim 20$. We can estimate the dependence of x_* on l_e when l_e is large and x_* is close to unity. If $\Gamma \leq 2$ and $l_e \gg 1$, $\alpha \approx 1$, and the photon density may be roughly approximated by

$$n(x) \approx \frac{3L_e}{4\pi R^2 m_e c^3} \frac{1 + \tau_T/3}{\ln(x_*/x_s)} x^{-2}, \quad x \leq x_*, \quad (37)$$

where the coefficient multiplying x^{-2} ensures that

$$(4\pi R^3/3)m_e c^2 \int_{x_s}^{x_*} \dot{n}_{\text{esc}}(x) x dx = L_e,$$

and

$$n(x) \approx (1 + \tau_T/3) \dot{n}_{\text{esc}}(x) R/c.$$

Substituting equation (37) into equations (11) and (36), and

using equation (2a) and (10b) with PY = 0.1, we obtain

$$x_* \approx \max \left\{ 1, \frac{5(4\pi/3) \ln(x_*/x_s)}{l_e [1 + (0.4l_e/\pi)^{1/2}/3]} \right\}. \quad (38)$$

For values of x_* in the range we consider, equation (38) shows that x_* reaches unity at $l_e \approx 100$ and $\tau_T \approx 3.5$. For larger l_e , x_* remains ~ 1 because a photon with $x < 1$ can produce a pair only with photons with $x > 1$, which are already depleted by pair production (see the self-consistent solution in Appendix B). In Figures 1–3, the high-energy breaks occur at $x = x_{\max,1}$ for the low l_e models and at $x = x_*$ for the high l_e models.

ii) Breaks for $l_s/l_e \ll 1$

When $l_s/l_e \ll 1$, higher order (repeated) scatterings become relatively important and determine the location of the high-energy break in the spectrum. For power-law injections of electrons and sufficiently large Γ , the spectral break in this regime occurs at $x = 1$ (see the low l_s/l_e curves in Fig. 5). Under these conditions, a break at $x = 1$ occurs because that is the energy below which electrons of Lorentz factor about unity can scatter in the Thomson limit (see the upper limit of the integral in eq. [9] and its change in functional form at $x = 1$). This effect, which was first noted by Zdziarski and Lamb (1986), requires both that higher order scatterings dominate and that electrons of Lorentz factor ~ 1 dominate. The latter condition requires that $\Gamma > 1 + \alpha$.

For monoenergetic electron injection, or power-law injection with $\Gamma < 1 + \alpha$, the low Lorentz factor electrons do not sufficiently dominate, and the spectral break extends up to $x \approx \gamma_{\max}$ (see the low l_e/l_e models in Fig. 6). Even for $l_s/l_e > 1$, higher order scatterings can form a knee on the spectrum at energies above x_* or $x_{\max,1}$.

Independent of l_s/l_e , the spectrum cannot extend above the energy $x \approx x_*$ without breaking.

e) X-Ray Spectral Index

The X-ray spectral index α , defined by the least-squares fit to the spectrum between 2 and 10 keV, is shown for selected models in Tables 1 and 2. In general, α increases for increasing l_e (e.g., models A–E) and for increasing l_s/l_e (e.g., models N–P, g–i), but the dependence of α on these and other parameters is complex.

For monoenergetic electron injection satisfying inequality (34), with $l_e \lesssim 100$ (thermal Comptonization is not too

TABLE 2
RESULTS FOR SELECTED MODELS WITH POWER-LAW INJECTION^a

l_e	l_s/l_e	Γ	γ_{\max}	τ_T	θ	PY	l_s/l_e	α	x_*	Model
1	1	1.5	7.5×10^3	5.6×10^{-2}	1.6×10^{-2}	2.5×10^{-3}	3.9×10^{-2}	0.74	1.6×10^3	a
30	1	1.5	7.5×10^3	1.64	7.3×10^{-3}	7.0×10^{-2}	0.11	0.86	5.8	b
10^3	1	1.5	7.5×10^3	13.7	9.7×10^{-4}	0.15	0.13	1.4	1	c
10	3	0.5	400	0.73	5.4×10^{-3}	4.2×10^{-2}	7.0×10^{-2}	0.57	19	d
10	3	1.5	400	0.51	4.1×10^{-3}	2.1×10^{-2}	0.13	0.80	16	e
10	3	2.5	400	0.16	1.6×10^{-3}	2.0×10^{-3}	0.14	1.18	30	f
10	10^{-3}	2.5	7.5×10^3	1.0	0.18	7.3×10^{-2}	1.0×10^{-2}	0.30	2.2×10^3	g
10	3×10^{-2}	2.5	7.5×10^3	0.76	4.6×10^{-2}	4.5×10^{-2}	7.9×10^{-2}	0.68	20	h
10	5	2.5	7.5×10^3	0.19	1.1×10^{-3}	2.8×10^{-3}	0.13	1.20	33	i

^a $\gamma_{\min} = 1$, $x_s = 3 \times 10^{-5}$ for all models.

important), and $x_{\max,2} \gtrsim 1$, we expect α to lie in the range $0.5 \leq \alpha \leq 1.0$. The index α increases above unity even for a monoenergetic injection when the depletion of the spectrum due to Compton downscattering extends down to X-ray energies. Setting $1/\tau_T^2 \lesssim 0.03$, we obtain $\tau_T \gtrsim 6$ for this effect. At such large values of τ_T , l_e is large and PY has reached its asymptotic value of $\text{PY} \sim 0.1$. Then, using equation (20b) with $\tau_T = 6$ and $\text{PY} = 0.1$, we obtain $l_e \gtrsim 300$ for the condition that thermal Comptonization push α above unity. This is consistent with our results. (Note also, from Fig. 10, that $l_e \sim 300$ corresponds to $l_{\text{ob}} \sim 10$.)

Figure 4 and models d, e, and f show the sensitivity of α to Γ . For these models with low $x_{\max,2}$, pairs have little effect on the X-ray region of the spectrum, and α is controlled completely by the primary electron injection and the value of Γ .

Figures 5 and 6 and models N, O, P, and g-i show the sensitivity of α to l_s/l_e . For $l_s \ll l_e$, α is small. For increasing l_s/l_e , α increases, until it becomes independent of l_s/l_e for $l_s/l_e \gg 1$. Note also in Figure 6 that α is affected by secondary electron injection for high l_s/l_e , but not for low l_s/l_e , where higher order scatterings dominate and smooth out the spectrum.

Finally, Figure 7 and models L and M show the sensitivity of α to x_s . When x_s is increased from 10^{-5} to 3×10^{-5} , the Compton upscattered photons enter the lower portion of the X-ray band and increase α .

f) Pair Yield

Figure 8 shows the pair yield for a several groups of models. Monoenergetic injection models with the same values of x_s and γ_{\max} but different l_s/l_e give about the same results. As can be seen, PY is approximately linear with l_e for $l_e \ll 1$, in accordance with equation (16), rises rapidly in the range $2 \lesssim l_e \lesssim 7$, and saturates at a value $\text{PY} \approx 0.1$ for $l_e \gtrsim 10$, as first found by S87. The rise of PY in the region $2 \lesssim l_e \lesssim 7$ is not as sharp in our calculations as in those of S87. This is because we use a distributed soft photon input, rather than a δ -function, and also allow for higher order Compton scatterings.

The dotted curve represents a model with a power-law injection with parameters the same as in Figure 3. The rise of PY is smoother than for monoenergetic injection (no "pair runaway"), but PY saturates at a similar value (see Table 2 for PY for other power-law models).

g) Comparison to Previous Calculations

We computed models with $x_s = 10^{-4}$, a monoenergetic injection at $\gamma_{\max} = 10^3$, $l_s/l_e = 1$, and $l_e = 40$ and 400, corresponding to models 2 and 5 of FBGPC86. For the $l_e = 40$ model, we obtained $\text{PY} = 8.9 \times 10^{-2}$, $\Theta = 7 \times 10^{-3}$,

$\alpha = 0.80$, and $\tau_T = 2.1$, while FBGPC86 obtained $\text{PY} = 5.7 \times 10^{-2}$, $\Theta = 1.1 \times 10^{-2}$, $\alpha = 0.76$, and $\tau_T = 1.75$. For the $l_e = 400$ model, we obtained $\text{PY} = 0.15$, $\Theta = 2 \times 10^{-5}$, $\alpha = 0.97$, and $\tau_T = 8.8$, while FBGPC86 obtained $\text{PY} = 6.7 \times 10^{-2}$, $\Theta = 2.1 \times 10^{-3}$, $\alpha = 0.97$, and $\tau_T = 5.97$. Thus, our pair yields are somewhat higher, but the quantitative agreement is pretty good. However, the detailed spectra are different, as can be seen in Figure 9a for the $l_e = 400$ model. Here the FBGPC spectrum converted to our units is shown by the dashed curve. Their spectrum is much more depleted than ours at $x > 1/\tau_T^2$, due to their approximation that a photon at $x \ll 1$ has a mean escape time of $\tau_T R/c$ (where we use $\tau_T R/3c$ in eq. [21a]) and their neglect of the relativistic corrections $f(x)$ and $\omega(x)$ (see eqs. [21b] and [22c]). At $x = 1$, for example, with $\tau_T \approx 9$, the relativistic correction $f(x)$ decreases the effective value of τ_T by a factor 4 or a factor 10,

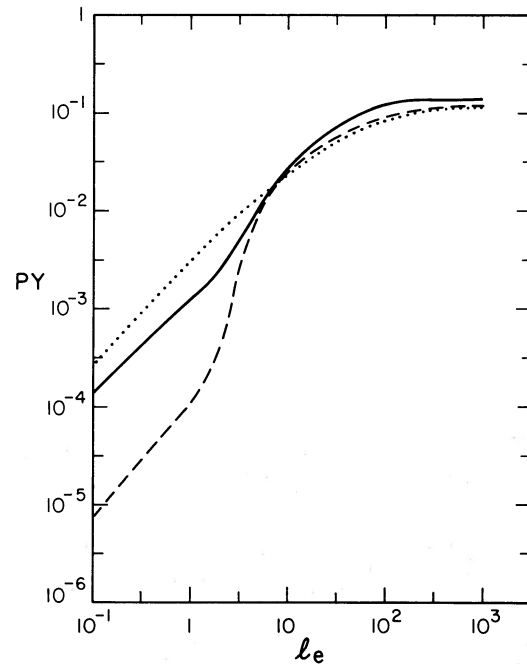


FIG. 8.—The pair yield, PY, as a function of l_e for various models. Models with monoenergetic electron injection are given by solid curve, with $\gamma_{\max} = 1.2 \times 10^3$ and $l_s/l_e = 0.25$, and dashed curve, with $\gamma_{\max} = 7.5 \times 10^3$, $l_s/l_e = 2.5$. Dotted curve represents a model with power-law electron injection and $\gamma_{\max} = 7.5 \times 10^3$, $\Gamma = 2$, $l_s/l_e = 1$. For all models, $x_s = 3 \times 10^{-5}$. Changing Γ from 2 to 1.5 in the power-law model leaves the resulting curve almost unchanged. Also the pair yield does not depend much on l_s/l_e .

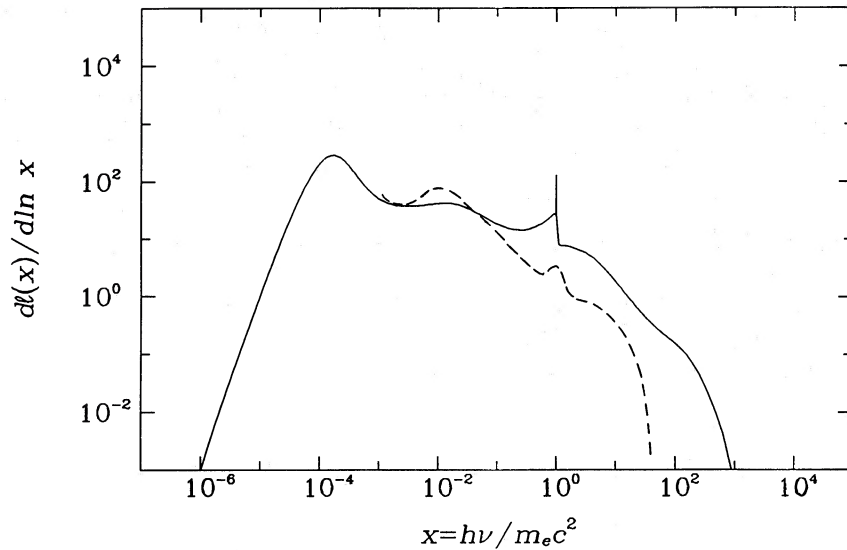


FIG. 9a

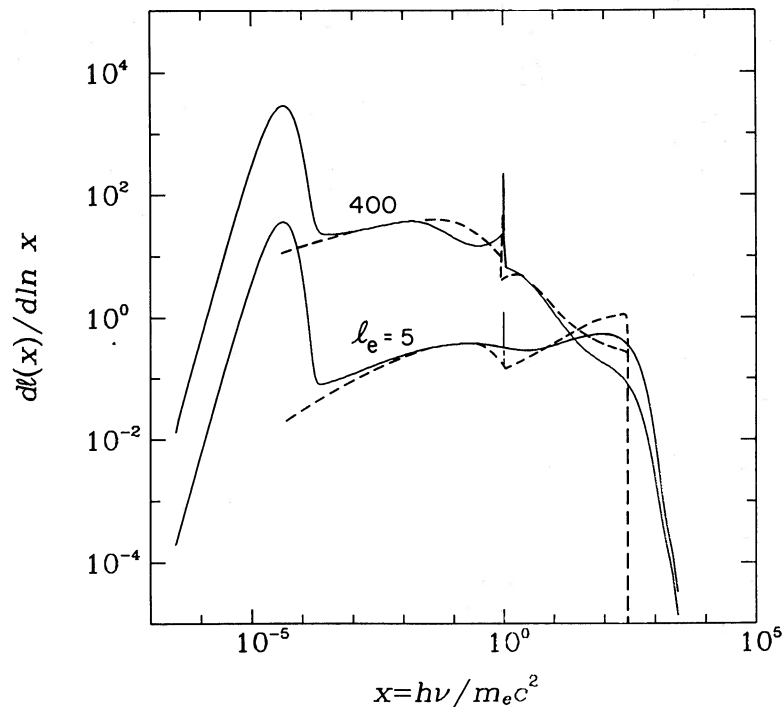


FIG. 9b

FIG. 9.—Comparisons to previous calculations for monoenergetic electron injection. (a) $x_s = 10^{-4}$, $\gamma_{\max} = 1000$, $l_s/l_e = 1$, $l_e = 400$. Dashed curve is from Fabian *et al.* (1986); solid curve is ours. See text for discussion. (b) $x_s = 3 \times 10^{-5}$, $\gamma_{\max} = 3000$, $l_s/l_e = 10$, and $l_e = 400$ and 5, as indicated. Dashed curves are from Svensson (1987); solid curves are ours. See text for discussion, and Table 1, models I, J, and K.

depending on whether $\tau_T/3$ or τ_T is used in equation (21a), and the relativistic correction ω decreases the effective value of τ_T by another factor of 6. Without these relativistic corrections, the spectrum at $x = 1$ is depleted below ours by more than a factor of 20. Because FBGPC86 continue using $\tau_T R/c$ as the photon escape time even for $x > 1$, their spectra remain significantly depleted below ours in this energy range. The FBGPC86 spectrum drops very abruptly at high energies, where pair production is important, because they reduce their emergent spectra by the factor $e^{-\tau_T \gamma}$ (Fabian, private

communication), rather than the factor $\sim 1/\tau_T \gamma$ given by solving equations (3) and (21a). The latter factor is appropriate for photon production distributed throughout the pair production region.

We also computed models with $x_s = 2.7 \times 10^{-5}$, $\gamma_{\max} = 3 \times 10^3$, $l_s/l_e = 10$, and $l_e = 5$ and 400, corresponding to two models calculated in S87. We obtained almost identical values for the pair yields. For $l_e = 5$ and 400, $\tau_T = 0.3$ and 7.2, respectively. Since Svensson determines Θ only crudely, a comparison here is not useful. Figure 9b shows a comparison between

our spectra and Svensson's for these two models. The discrepancies can be explained by the differences in our treatments of Comptonization and of the distribution of \dot{n}_0 . In the region $1/\tau_T^2 \lesssim x \lesssim 0.3$, our spectrum is more depleted than that of Svensson's. One contribution to this discrepancy derives from the difference in our treatments of the distribution of photon sources: we assume the photon sources are distributed sinusoidally, reflected in our use of equation (21a), while Svensson assumes they are distributed uniformly (see Sunyaev and Titarchuk 1980). A second contribution is the difference between our treatments of Comptonization. Like the spectra of FBGPC86, Svensson's spectra are more depleted than ours at $0.3 \lesssim x \lesssim 1$ due to his neglect of relativistic corrections to the escape and scattering probabilities. The sharp dip of the spectra at $x = x_{\max,2}$ (equal to unity for this particular choice of parameters) and at $x = x_{\max,1}$ in Svensson's models arise from his assumptions that *both* the primary electron injection *and* the soft photon injection are monoenergetic. For $x_s = 2.7 \times 10^{-5}$ and $\gamma_{\max} = 3 \times 10^3$, $x_{\max,2} = 0.95$, and photon production by secondary pair injection stops abruptly at $x \geq 0.95$. However, for a *distributed* soft photon input, such as our blackbody peaked at x_s , some soft photons are injected above and below $x = x_s$ and the feature at $x = x_{\max,2}$ is not nearly so pronounced. For the same reason, our spectra do not drop abruptly to zero at $x = x_{\max,1}$, but extend beyond this point. The amplitudes of our spectra in the region $x_* < x$ fall below those of Svensson's because we evaluate τ_{yy} at photon densities characteristic of a mean interior point of the emitting region, while Svensson evaluates τ_{yy} at escaping photon densities. The latter densities are lower, causing a smaller depletion in photons from pair production. The detailed shape of the spectra in this energy range are not reliable, and more work is needed on radiative transfer in pair media.

h) The Reduced Eddington Limit

Combining equations (30) and (31) for $2n_+/n_i \gg 1$ and $PY \approx 0.1$, we obtain, at $R = 2R_s$,

$$\frac{L}{L_E^*} = 0.1 l_e^{1/2} \frac{\epsilon_{0.1}}{\mu}. \quad (39)$$

This can also be written as a function of l_{ob} . As can be seen in Figure 10, for $l_e \gtrsim 10$, l_{ob} is almost exclusively a function of l_e and becomes independent of l_s/l_e , x_s , γ_{\max} , and the form of the injection. In models N, O, and P, for example, where l_s/l_e varies over a factor 10^3 , l_{ob} varies only from 0.79 to 2.2. This delightful simplification arises because both l_s/l_e and PY approach ~ 0.1 for $l_e > 10$, independent of other parameters. Since $\tau_T \propto (l_e PY)^{1/2}$, $l_{\text{ob}} \propto l_e^{1/2}$ for $l_e \gtrsim 10$ (see eq. [2e]). Thus, for $l_e \gtrsim 50$ and $L/L_E^* \lesssim 1$, we obtain

$$\frac{L}{L_E^*} \approx 0.3 l_{\text{ob}} \frac{\epsilon_{0.1}}{\mu}. \quad (40)$$

V. COMPARISON TO OBSERVATIONS

a) Data without Theory

We have compiled the available data on the X-ray spectral indices, luminosities, and variability time scales of AGNs and QSOs (not including BL Lac objects) in Table 3. Shown also are the computed observed compactness parameters l_{ob} as defined in equation (2d). Figure 11 gives the positions of these objects in the two-dimensional $\alpha - l_{\text{ob}}$ plane.

Without application of any theory at all, Table 3 and

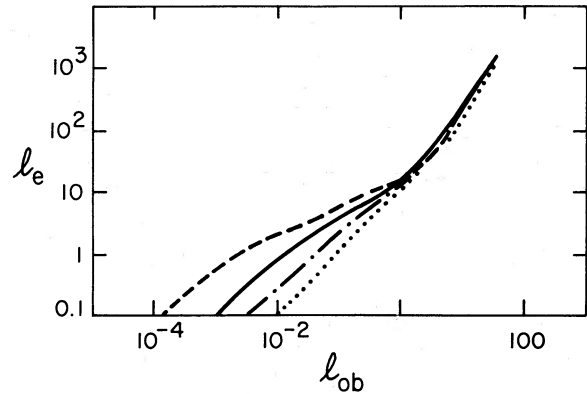


FIG. 10.—Electron compactness parameter l_e as a function of the observed compactness parameter l_{ob} for several groups of models. Groups 1–4 are models with monoenergetic electron injection and are defined as follows: $(l_s/l_e, \gamma_{\max}) = (2.5, 1.2 \times 10^3)$ in group 1, $(2.5, 7.5 \times 10^3)$ in group 2, $(0.25, 7.5 \times 10^3)$ in group 3, and $(0.25, 1.2 \times 10^3)$ in group 4. Groups 5 and 6 are models with power-law electron injection, $l_s/l_e = 1$ and $\gamma_{\max} = 7.5 \times 10^3$, with $\Gamma = 2$ (model 5) and $\Gamma = 1.5$ (model 6). In all groups, $x_s = 3 \times 10^{-5}$. Dashed curve refers to groups 2 and 3, solid curve to groups 1 and 4, dotted curve to group 5, and dash-dotted curve to group 6.

Figures 11 and 12 suggest the following: (1) There is little correlation between α and l_{ob} . (2) The spectral index α varies broadly from ~ 0.4 to ~ 1.0 . Ten of the 23 objects have values of α lying outside the range $\alpha = 0.67 \pm 0.15$ found in the samples of Mushotzky *et al.* (1980), Rothschild *et al.* (1983), and Petre *et al.* (1984). Thus, it may be misleading to interpret

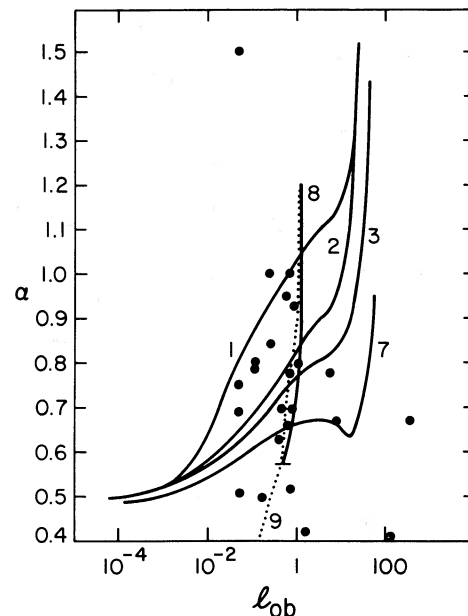


FIG. 11.—Comparisons of theory to observations for X-ray spectral index α as a function of observed compactness parameter l_{ob} . Positions of AGNs and QSOs in the $\alpha - l_{\text{ob}}$ plane are indicated by dots. Curves are theoretical. Curves labeled by "1," "2," and "3" correspond to the groups of monoenergetic injection models 1, 2, and 3 defined in Fig. 10. The group of models labeled by "7" have the same parameters as group 3, except that $l_s/l_e = 0.05$. Curves labeled by "8" and "9" are power-law electron injection models. Models in group 8 have $l_e = 10$, $x_s = 3 \times 10^{-5}$, $l_s/l_e = 3$, and $\gamma_{\max} = 400$, with varying Γ . Models in group 9, which are given by a dotted curve to help distinguish them from group 8, have $l_e = 10$, $x_s = 3 \times 10^{-5}$, $\gamma_{\max} = 7.5 \times 10^3$, and $\Gamma = 2.5$, with varying l_s/l_e . Bar at the bottom of the group 8 curve marks the lowest possible value of α for these models.

TABLE 3
DATA FROM AGNs AND QSOs

Name	α	$\log L_x$	$\log \Delta t$	Type	l_{ob}	Spectral Data References	Luminosity/ Time Variability References
NGC 526A	0.52	43.85	4.9	SII/NELG	0.75	1	1
NGC 2110	0.80	43.08	4.9	SII/NELG	0.12	1	1
NGC 2992	0.79	43.25	5.1	SII/NELG	0.12	1	1
NGC 3031	1.5	40.48	2.7	SI	0.054	2	1
NGC 3227	0.51	42.11	4.3	SI	0.054	1	1
NGC 3516	0.7	42.70	4.0	SI	0.45	3	1
NGC 4051	1.0	41.48	3.0	SI	0.27	4	1
NGC 4151	0.50	42.85	4.6	SI	0.16	1	1
NGC 4593	0.67	43.41	3.4	SI	8.6	1	1
NGC 5506	0.75	43.00	5.2	SII/NELG	0.052	1	1
NGC 6814	0.42	41.25	2.0	SI	1.6	1	1
NGC 7314	...	42.60	3.3	SI	1.8	1	2
NGC 7469	0.78	43.81	4.9	SI	0.73	1	1
NGC 7582	0.69	42.55	4.8	SII/NELG	0.049	1	1
III Zw 2	0.67	44.90	3.3	SI	360	5	2
F9	0.95	44.34	5.5	SI	0.57	6	1
4U 0241+62	0.66	44.30	5.4	QSO	0.70	6	1
MCG -5-23-16	0.84	43.48	5.0	SII/NELG	0.25	1	1
MCG -6-30-15	...	42.95	3.3	SI	3.8	1	2
3C 273	0.41	46.22	5.1	QSO	119	1	1
3C 382	0.93	44.40	5.4	BLRG	0.88	1	1
OX 169	...	44.20	4.4	QSO	6.2	1	1
AKN 120	...	44.26	3.4	SI	73	1	2
Mrk 205	0.8 ^a	44.45	5.4	QSO	1.13	7	1
Mrk 335	0.78	43.60	3.8	SI	5.8	1	2
Mrk 509	0.63	44.36	5.7	SI	0.41	1	1
Mrk 766	...	42.34	3.9	SI	0.28	1	1
Mrk 841	0.7	43.92	5.0	QSO	0.84	8	1

^a 0.2–3.5 keV.

REFERENCES.—For spectral data: (1) Mushotzky 1984, and references therein; (2) Barr and Mushotzky 1987; (3) Reichert, Barr, and Mushotzky 1987; (4) Lawrence *et al.* 1985; (5) Petre *et al.* 1984; (6) Pounds *et al.* 1985; (7) Wilkes and Elvis 1987; (8) Arnaud *et al.* 1985. For luminosity ($H_0 = 50$) and time variability data, (1) Wandel and Mushotzky 1986, and references therein; (2) Warwick 1986, and references therein.

the data in terms of a “universal” value of spectral index, $\alpha \approx 0.7$. A similar point has been made by Wilkes and Elvis (1987). Also, $\alpha = 0.7$ spectra must harden toward hard X-rays and γ -rays in objects with large $L_{0.5-5 \text{ MeV}}/L_x$. This ratio is $\gtrsim 10^2$ for most objects with measured γ -ray luminosities (e.g., MCG 8–11–11, NGC 4151; Bassani and Dean 1983, and references therein), implying $\alpha_{x-\gamma} \lesssim 0.3$. (3) Ignoring the three extreme objects AKN 120, 3C 273, and III Zw 2, the observed compactness parameters have an upper limit of $l_{ob} \lesssim 10$. It

seems important to test this apparent upper limit against new observations.

b) Constraints from High-Energy Break

From the theoretical curves in Figure 11, it is clear that a wide range of input parameters is needed to fit the range of data from one object to the next. The two extreme objects (III Zw 2 and 3C 273) may not be fitted by any models of the type we have considered.

Critical constraints on all models are provided by the requirements that the high-energy break occur at $x \lesssim 5-10$ and $\alpha_\gamma \gtrsim 1.5-2.0$, requirements imposed by the observed upper limits (Perotti *et al.* 1981a, b; Hermsen *et al.* 1981; Pollock *et al.* 1981) and considerations of the γ -ray background (e.g., Bignami *et al.* 1979; Bassani and Dean 1983). The spectra of three of the AGNs with the largest apparent brightnesses, Cen A, NGC 4151, and MCG 8–11–11, as well as of 3C 120, have been observed to break at these energies (Bignami *et al.* 1979; Graml, Penningsfeld, and Schönfelder 1978; Perotti *et al.* 1981b; Damle *et al.* 1986), and it is possible that most of them do. The γ -ray observations of 3C 273, if extrapolated to lower energies, also indicate a spectral break at $\sim 3 \text{ MeV}$ (Bignami *et al.* 1979). The typical object in Figures 11 and 12 has $l_{ob} \sim 0.5$, corresponding to $l_e \sim 10$, and a value of α ranging from 0.5 to 1.0, NGC 4151, MCG 8–11–11, and Cen A all have $l_{ob} \leq 1$ (Bassani and Dean 1983). With such a modest value of l_e , $x_* > 30$ and pair absorption does not break

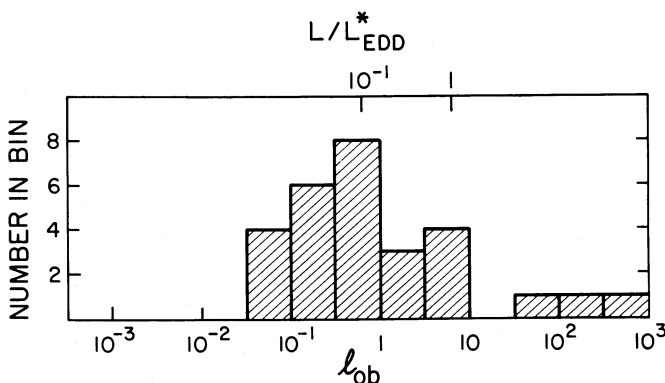


FIG. 12.—Histogram of observed compactness parameters. Top abscissa is labeled with some values of L/L_E^* corresponding to the value of l_{ob} , using $R = 2R_s$, $\epsilon_{0.1}/\mu = 0.5$.

the spectrum at a sufficiently low energy. An appropriate spectral break caused by pair absorption would require $l_e \gtrsim 50$, which in turn requires $l_{ob} \gtrsim 3$. (Note, however, that NGC 4151, MCG 8-11-11, and Cen A have $l_e/l_{ob} \gtrsim 10^2$; Bassani and Dean 1983.) This in turn requires that the size of the typical emitting region, R , must be more than 6 times smaller than the value $R = c\Delta t/(1 + \tau_T/3)$ used in our calculations. Furthermore, when pair production *does* cause a break in the spectrum, it steepens the spectrum by a factor $1/\tau_{\gamma\gamma} \propto x^{-\alpha}$ (unless pairs are absorbed outside the source), which is less than the observed steepening in the objects mentioned above and probably not sufficient in most AGNs to conform to the limits of the γ -ray background.

For these reasons, we consider it unlikely that pair production is the source of the high-energy break in the typical AGN. Thus, in the models we consider, the break must be provided either by (1) a small value of the maximum photon energy from first-order scattering by primary electrons, which requires $3 \lesssim x_{\max,1} \lesssim 10$, or by (2) a domination of higher order scatterings and electrons of low Lorentz factor, which requires $l_s/l_e \ll 1$ and $\Gamma > 2.5-3$, where the latter condition ensures that the break will be steep enough (see discussion in §§ IVc, d.) Models can be classified according to which of these two mechanisms provides the high-energy spectral break.

c) Variable Γ Models

When the high-energy break is provided by a small value of $x_{\max,1}$, the required variation in α can be achieved by a variation in Γ , $1 \lesssim \Gamma \lesssim 2.5$. Such models are shown as the curve labeled "8" in Figure 11 and the spectra in Figure 4 (models d, e, and f in Table 2), where parameters have been chosen to give typical observed values of l_{ob} as well as a suitable high-energy break. Although a universal value of $x_{\max,1} \approx 3-10$ may not be too plausible, a range of Γ is. Recently, Takahara (1986) found a strong dependence of Γ obtained from shock acceleration on the motion and distribution of scattering centers, suggesting that shock acceleration produces no universal index Γ .

Several features and restrictions of these models are important. First, l_s/l_e cannot be too small, or else higher order scatterings will dominate, and, when $\Gamma \lesssim 1.5-2$, the high-energy break will extend up to γ_{\max} and be too large. Second, these models cannot produce values of α below ~ 0.6 (see the bar at the bottom of curve 8 in Fig. 11). This is because, for $l_e \gtrsim 10$, pairs will always increase α somewhat above 0.6 (see discussion in § IVb). Thus for AGNs with $0.4 \lesssim \alpha \lesssim 0.6$ these models will not apply. Third, pairs are not very important in contributing to the X-ray spectra of these models. In order to fit the observed power-law form of the spectra, $x_{\max,2}$ cannot lie in the X-ray band, where it would cause a noticeable dip and a departure from a power-law form; $x_{\max,2}$ must be either much larger or much smaller than ~ 0.01 . However, with $x_{\max,1} \approx 3-10$, $x_{\max,2}$ could not be larger than 0.01 without x_s extending well above UV energies (see eqs. [15b] and [35]), where strong soft photon sources have not been observed. Thus $x_{\max,2}$ must lie

below the X-ray region of the spectrum. Since this is the maximum energy where pairs contribute to the spectrum, pairs cannot contribute much to the X-ray spectrum in these models. Finally, if a break energy of $x \approx 6$ proves to be a common feature of AGNs, one is left to explain why $x_{\max,1}$ falls naturally around this value.

d) Variable l_s/l_e Models

When the high-energy break is provided by a small value of l_s/l_e , the required variation in α can be achieved by a variation in l_s/l_e , $10^{-3} \lesssim l_s/l_e \lesssim 1$. Such a variation could result, for example, from a variation in the relative volumes in which the soft photons and γ -ray photons are produced. These models are represented in the dashed curve labeled "9" in Figure 11 and in the spectra in Figure 5 (models g-i in Table 2), where, again, parameters have been chosen to give typical observed values of l_{ob} .

As in the variable Γ models, several features and restrictions apply here as well. First, Γ must be large, $\Gamma \gtrsim 2.5-3.0$. If this condition is not satisfied, the γ -ray spectrum at energies above the break will not fall steeply enough to accommodate the limits given by the γ -ray background, as previously mentioned. Second, the spectral break will occur at $x \approx 1$. If the typical AGN has a spectral break at $x \approx 6 = 3$ MeV, as do Cen A, NGC 4151, MCG 8-11-11, and possibly 3C 273, then this class of models may be ruled out. And third, as in the variable Γ models, pairs do not contribute much to the X-ray region of the spectrum. For the large values of Γ required by these models, most of the injected energy is at $\gamma \approx 1$.

e) Possible Role of Pairs in Controlling the Luminosity

From the above discussion, it seems probable that pair production is not very important in the shape or high-energy break of the spectra from *typical* AGNs. (Pairs may certainly be much more important for the smaller number of high l_{ob} objects.) We suggest here that pairs may still be important in regulating the maximum luminosities of these objects, by reducing the Eddington limit.

We have labeled the upper x -axis of Figure 12 with the value of L/L_E^* corresponding to l_{ob} , assuming $R/2R_S = 1$, $\epsilon_{0.1}/\mu = 0.5$, and using equation (40). Except for the three extreme objects AKN 120, 3C 273, and III Zw 2, the AGNs and QSOs in our sample obey $L \lesssim L_E^*$. Unless $l_s/l_e \gg 1$, this upper limit to L may be a factor ~ 10 lower than the classical Eddington limit (see eq. [33]). Note that at this upper limit, where $l_{ob} \approx 5$ and $l_e \approx 100$, x_* is very close to unity, and, as long as $x_{\max,1} > 1$, pair effects can provide the high-energy break to the spectrum.

We are grateful to Martin Elvis and Leonid Ozernoy for helpful discussions, to Richard Mushotzky for helping us compile some of the data, and to Roland Svensson for sending us an early draft of his 1987 paper. One of us (A. A. Z.) was supported in part by the NSF grants AST 84-15355 and AST 84-51725.

APPENDIX A

ENERGY CONSERVATION

We now demonstrate that equations (3) and (4) and the various expressions for the quantities therein conserve total energy. Integrating equation (3) over $x dx$ and using equations (19), (9), (27), (10), the total escaping energy, per unit volume, per unit time, is

$$\int x \dot{n}_{\text{esc}} dx = \int x \dot{n}_0 dx + \int P(\gamma) d\gamma + \frac{4}{3} \sigma_T c \iint \gamma^2 x n(x) N(\gamma) H\left(\frac{3}{4} - x\gamma\right) d\gamma dx - c \sigma_T \int n(x) x N(\gamma) H\left(\frac{3}{4} - x\gamma\right) dx d\gamma - \frac{c}{R} \int x n(x) \tau_{\gamma\gamma}(x) dx. \quad (\text{A1})$$

The second term on the right-hand side of equation (A1) assumes that $\Theta = 0$, which neglects the thermal energy in electrons and positrons. This energy never exceeds $\sim 10^{-2}$ of the total energy, and we have neglected it in our calculations.

Now, using equation (6), and integrating by parts, we obtain

$$- \int_1^{\gamma_{\text{max}}} \dot{\gamma} N(\gamma) d\gamma = \int_1^{\gamma_{\text{max}}} [Q(\gamma) + P(\gamma)] (\gamma - 1) d\gamma, \quad (\text{A2})$$

and, using equation (7) for $\dot{\gamma}$, this is equal to the third and fourth terms on the right-hand side of equation (A1). Thus, we have

$$\int x \dot{n}_{\text{esc}} dx = \int x \dot{n}_0 dx + \int_1^{\gamma_{\text{max}}} [(\gamma - 1)Q(\gamma) + \gamma P(\gamma)] d\gamma - \frac{c}{R} \int_{1/\gamma_{\text{max}}}^{\gamma_{\text{max}}} x n(x) \tau_{\gamma\gamma}(x) dx. \quad (\text{A3})$$

Now, using equations (12) and (13), we have

$$\int_1^{\gamma_{\text{max}}} \gamma P(\gamma) d\gamma = \frac{c}{R} \int_1^{\gamma_{\text{max}}} \left(x + \frac{1}{x}\right) n(x) \tau_{\gamma\gamma}(x) dx, \quad (\text{A4})$$

and, using the expression for $\tau_{\gamma\gamma}$ in equation (11) and making the substitution $x \rightarrow 1/x$ in one of the two terms on the right-hand side of equation (A4), we finally obtain

$$\int_1^{\gamma_{\text{max}}} \gamma P(\gamma) d\gamma = \frac{c}{R} \int_{1/\gamma_{\text{max}}}^{\gamma_{\text{max}}} x n(x) \tau_{\gamma\gamma}(x) dx, \quad (\text{A5})$$

giving

$$\int x \dot{n}_{\text{esc}} dx = \int x \dot{n}_0 dx + \int_1^{\gamma_{\text{max}}} Q(\gamma) (\gamma - 1) d\gamma. \quad (\text{A6})$$

The right-hand side of equation (A6) is the injected energy, per unit time, per unit volume, in soft photons and in particles, respectively. Thus the emitted energy equals the injected energy.

APPENDIX B

NUMERICAL METHOD

In the absence of thermal Comptonization, equation (3) may be written as

$$n(x) = \frac{R}{c} \frac{\dot{n}_0 + \dot{n}_A + \dot{n}_C^{\text{NT}}}{(1 + (1/3)\tau_{\text{KN}} f)^{-1} + \tau_C^{\text{NT}} + \tau_{\gamma\gamma}}. \quad (\text{A7})$$

Since the terms on the right-hand side may be written as functions of $n(x)$ and integrals over $n(x)$, equation (A7) represents a complex integral equation for $n(x)$. In our first stage of solution, we solve equation (A7) by successive iterations. The right-hand side is evaluated at an old $n(x)$, then a new $n(x)$ is computed by equation (A7), and so on. Using this scheme, however, we find that basing $\tau_{\gamma\gamma}(x)$ on the old $n(x)$ in order to determine the new $n(x)$ leads to difficulties with convergence. Fortunately, the special form of $\tau_{\gamma\gamma}$ allows an exact, self-consistent solution for $n(x)$ and $\tau_{\gamma\gamma}(x)$, given the other quantities in equation (A7) as fixed functions of x . First, write equation (A7) in the form

$$n(x) = \frac{A(x)}{B(x) + C(x)n(1/x)}, \quad (\text{A8a})$$

where $\tau_{\gamma\gamma} = C(x)n(1/x) = 0.2R\sigma_T x^{-1}n(1/x)$. Next, change x to $1/x$ in equation (A8a), obtaining

$$n\left(\frac{1}{x}\right) = \frac{D(x)}{E(x) + F(x)n(x)}, \quad (\text{A8b})$$

where $D(x) \equiv A(1/x)$, $E(x) \equiv B(1/x)$, $F(x) \equiv C(1/x)$, and A, B, C, D, E, F are all known functions of x . Substituting equation (A8b) into equation (A8a) then yields a quadratic equation for $n(x)$. Taking the positive root, gives us $n(x)$ and $\tau_{\gamma\gamma}(x)$. Using this method for n and $\tau_{\gamma\gamma}$ at each iteration, 5–10 iterations on equation (A7) produce convergence at better than 1%.

In our second stage, we include the effects of thermal Comptonization. This is done by numerically solving equations (3), (22), and (23), with $\dot{n}_0, \dot{n}_A, \dot{n}_C^{\text{NT}}, \tau_C^{\text{NT}}, \tau_{\gamma\gamma}$, and τ_T given functions of x , as determined by the last iteration in stage 1. After solving for $n(x)$ in this way, an equilibrium temperature Θ is computed by equation (28). This Θ is not self-consistent, however, because an estimated Θ had to be used to solve equation (22). Furthermore, $\tau_{\gamma\gamma}(x)$ and $n(x)$ are not self-consistent, leading to numerical instabilities. Therefore, we calculate a new $\tau_{\gamma\gamma}(x)$ based on the new $n(x)$, use the new Θ , and again solve equations (3), (22), and (23), with $\dot{n}_0, \dot{n}_A, \dot{n}_C^{\text{NT}}, \tau_C^{\text{NT}}$, and τ_T unchanged. This process is repeated typically 5 times, updating $\tau_{\gamma\gamma}$ and Θ at each iteration, until convergence at better than 1% is achieved.

In our third stage of solution, we recalculate $\dot{n}_A, \dot{n}_C^{\text{NT}}, \tau_C^{\text{NT}}, \tau_{\gamma\gamma}$, and τ_T based on the latest $n(x)$. After this, equations (3), (22), and (23) are solved again, including the iterations on Θ and $\tau_{\gamma\gamma}$ described for the second stage. Stage 3 is repeated ~ 5 times, until all quantities have converged to better than 1%. Note that after the first stage, equation (A7) is no longer used because it neglects thermal Comptonization.

The two boundary conditions used to solve the Kompaneets equation are

$$\Theta \frac{du}{dx} + u = 0$$

at the lowest x , expressing zero flux, and

$$u = [n_0 + \dot{n}_C^{\text{NT}} + (1 - f_\theta)\dot{n}_A]/(\tau_{\gamma\gamma} + \tau_C^{\text{NT}} + \tau_{\text{KN}} + 1)$$

at $x = 1$, resulting from the solution of equations (3), (21), and (23) in the region $x \geq 1$.

In actual computations, the value of x dividing the regime of equation (22a) and the regime of equation (23) was taken as $x \approx 1.1$ – 1.5 rather than $x = 1$, so that the transition in calculational method would not interfere with a good treatment of the annihilation line at $x = 1$. For the transition value of x, x_t , not equal to unity, the ωn term in the numerator of equation (28) must be evaluated at x_t and multiplied by x_t^3 ; in the denominator it must be evaluated at x , and multiplied by x_t^2 .

REFERENCES

- Arnaud, K., et al. 1985, *M.N.R.A.S.*, **217**, 105.
 Barr, P., and Mushotzky, R. F. 1987, in preparation.
 Bassani, L., and Dean, A. J. 1983, *Space Sci. Rev.*, **37**, 367.
 Bechtold, J., Czerny, B., Elvis, M., Fabbiano, G., and Green, R. F. 1987, *Ap. J.*, **314**, 699.
 Begelman, M. C. 1979, *M.N.R.A.S.*, **187**, 237.
 Begelman, M. C., Sikora, M., and Rees, M. J. 1987, *Ap. J.*, **313**, 689.
 Bignami, G. F., Fichtel, C. E., Hartman, R. C., and Thompson, D. J. 1979, *Ap. J.*, **232**, 649.
 Cooper, G. 1971, *Phys. Rev. D*, **3**, 2312.
 Damle, S. V., et al. 1986, *Adv. Space Res.*, Vol. 6, No. 4, p. 173.
 Elvis, M., Green, R. F., Bechtold, J., Schmidt, M., Neugebauer, G., Soifer, B. T., Matthews, K., and Fabbiano, G. 1986, *Ap. J.*, **310**, 291.
 Fabian, A. C., Blandford, R. D., Guilbert, P. W., Phinney, E. S., and Cuellar, L. 1986, *M.N.R.A.S.*, **221**, 931 (FBGPC86).
 Gould, R. J., and Schröder, G. P. 1967, *Phys. Rev.*, **155**, 1404.
 Graml, F., Penningfeld, F. P., and Schönfelder, V. 1978, in *Proc. Symposium on Gamma-Ray Spectroscopy in Astrophysics* (NASA TM 79619), p. 207.
 Guilbert, P. W. 1986, *M.N.R.A.S.*, **218**, 171.
 Guilbert, P. W., Fabian, A. C., and Rees, M. J. 1983, *M.N.R.A.S.*, **205**, 593.
 Hall, R. D., Meegan, C. A., Walraven, G. D., Rjuth, F. T., and Haymes, R. C. 1976, *Ap. J.*, **210**, 631.
 Hermsen, W., et al. 1981, *Proc. 17th Internat. Cosmic-Ray Conf.* (Paris), **1**, 230.
 Herterich, K. 1974, *Nature*, **250**, 311.
 Jauch, J. M., and Rohrlich, F. 1980, *The Theory of Photons and Electrons* (New York: Springer).
 Jelley, J. V. 1966, *Nature*, **211**, 472.
 Kazanas, D. 1984, *Ap. J.*, **287**, 112.
 Lawrence, A., Watson, M. G., Pounds, K. A., and Elvis, M. 1985, *M.N.R.A.S.*, **217**, 685.
 Lightman, A. P., and Zdziarski, A. A. 1987, in preparation.
 Lightman, A. P., Zdziarski, A. A., and Rees, M. J. 1987, *Ap. J. (Letters)*, **315**, L113.
 Malkan, M. A., and Sargent, W. L. W. 1982, *Ap. J.*, **254**, 22.
 Moskalik P., and Sikora, M. 1986, *Nature*, **319**, 649.
 Mushotzky, R. F. 1982, *Ap. J.*, **256**, 92.
 ———. 1984, *Adv. Space Res.*, Vol. 3, Nos. 10–12, p. 157.
 Mushotzky, R. F., Marshall, F. E., Boldt, E. A., Holt, S. S., and Serlemitsos, P. J. 1980, *Ap. J.*, **235**, 377.
 Perotti, F., Della Ventura, A., Villa, G., Di Cocco, G., Bassani, L., Butler, R. C., Carter, J. N., and Dean, A. J. 1981a, *Ap. J. (Letters)*, **247**, L63.
 Perotti, F., Della Ventura, A., Villa, G., Di Cocco, G., Butler, R. C., Carter, J. N., and Dean, A. J. 1981b, *Nature*, **292**, 133.
 Petre, R., Mushotzky, R. F., Krolik, J. H., and Holt, S. S. 1984, *Ap. J.*, **280**, 499.
 Pollock, A. M. T., Bignami, G. F., Hermsen, W., Kanbach, G., Lichti, G. G., Masnou, J. L., Swanenburg, B. N., and Wills, R. D. 1981, *Astr. Ap.*, **94**, 116.
 Pounds, K. A., McHardy, I. M., Stewart, G., and Warwick, R. S. 1985, in *X-Ray Astronomy 1984*, ed. M. Oda and R. Giacconi (Tokyo: Institute of Space and Astronautical Science), p. 409.
 Reichert, G., Barr, P., and Mushotzky 1987, in preparation.
 Ross, R. R., Weaver, R., and McCray, R. 1978, *Ap. J.*, **219**, 292.
 Rothschild, R. E., Mushotzky, R. F., Baity, W. A., Gruber, D. E., Matteson, J. L., and Peterson, L. E. 1983, *Ap. J.*, **269**, 423.
 Schönfelder, V. 1983, *Adv. Space Res.*, Vol. 3, No. 4, p. 59.
 Schultz, A. L., and Price, R. H. 1985, *Ap. J.*, **291**, 1.
 Sunyaev, R. A., and Titarchuk, L. G. 1980, *Astr. Ap.*, **86**, 121.
 Svensson, R. 1982, *Ap. J.*, **258**, 321.
 ———. 1983, *Ap. J.*, **270**, 300.
 ———. 1986, in *Radiation Hydrodynamics in Stars and Compact Objects*, ed. K.-H. Winkler and D. Mihalas (Berlin: Springer), p. 325.
 ———. 1987, *M.N.R.A.S.*, in press.
 Takahara, F. 1986, in *Internat. School and Workshop on Plasma Astrophysics*, ed. T. D. Guyenne and I. M. Zeleny (Paris: European Space Agency).
 von Ballmoos, P., Diehl, R., and Schönfelder, V. 1987, *Ap. J.*, **312**, 134.
 Wandel, A., and Mushotzky, R. F. 1986, *Ap. J. (Letters)*, **306**, L61.
 Warwick, R. S. 1986, in *The Physics of Accretion onto Compact Objects* ed. K. O. Mason, M. G. Watson, and N. E. White (Berlin: Springer), p. 195.
 Wilkes, B. J., and Elvis, M. 1987, *Ap. J.*, submitted.
 Zdziarski, A. A., and Lamb, D. Q. 1986, *Ap. J. (Letters)*, **309**, L79.
 Zdziarski, A. A., and Lightman, A. P. 1985, *Ap. J. (Letters)*, **294**, L79 (ZL85).

ALAN P. LIGHTMAN: Harvard-Smithsonian Center for Astrophysics, 60 Garden Street, Cambridge, MA 02138

ANDRZEJ A. ZDZIARSKI: 130–33 Theoretical Astrophysics, Caltech, Pasadena, CA 91125